RSC Applied Interfaces

ROYAL SOCIETY OF CHEMISTRY

PAPER

View Article Online
View Journal | View Issue

Cite this: *RSC Appl. Interfaces*, 2025, **2**, 261

Electrophoretically deposited artificial cathode electrolyte interphase for improved performance of NMC622 at high voltage operation†

Inbar Anconina and Diana Golodnitsky *

Received 16th September 2024,
Accepted 21st November 2024

DOI: 10.1039/d4lf00319e

rsc.li/RSCApplInter

High-voltage Ni-rich active materials are widely used in cathodes of high-energy-density lithium-ion batteries (LIBs). However, the high charge cutoff voltages lead to significant degradation and capacity fading, caused by electrolyte decomposition, transition metal dissolution, structural distortion, and more. Herein, we present an artificial cathode electrolyte interphase (ART-CEI) as a protective coating on the surface of the $LiNi_{0.6}Mn_{0.2}Co_{0.2}O_2$ (NMC622) cathode. A composite film, prepared from argyrodite Li_6PS_5Cl (LPSC) ion conducting nanoparticles and a polymerized ionic liquid (PIL) as a binder, was electrophoretically deposited on the surface of the cathode. We found that capacity retention at high-voltage operation (4.3 and 4.5 V) is improved due to the coating. Besides the stability improvement, the electrochemical performance of the coated cathode shows an enhancement in rate performance and lower resistances of the anode solid electrolyte interphase (SEI), the cathode electrolyte interphase (CEI), and charge transfer processes during cycling.

Introduction

Over the recent decades, there has been growing interest in researching high-energy-density battery technologies, particularly for electric vehicles (EVs).[1–4] High-voltage materials, such as Ni-rich lithium nickel manganese cobalt oxide (NMC) layered cathodes ($Li[Ni_xMn_yCo_{1-x-y}]O_2$, $0.6 \leq x$), are considered some of the most effective lithium-ion cathodes.[5–8] These cathodes combine the high capacity of nickel oxide, the fast kinetics of cobalt oxide, and the structural stability of manganese oxide, offering high practical capacities (150–210 mA h g^{-1}), a high operating voltage range (~3.0–4.5 V), a relatively long lifespan, and low cost and toxicity compared to conventional Co-based cathodes.[9–12] Hence, NMC cathodes are widely used in commercial applications.[13–16] However, like other layered structure cathodes, Ni-rich cathodes are prone to degradation over time.[17,18] The degradation mechanisms have been extensively studied and include electrolyte decomposition,[19,20] structural changes and irreversible phase transitions in the cathode,[21,22] dissolution of transition metal (TM) cations,[23,24] Li/Ni cation-mixing,[25,26] oxygen release,[27] residual inactive lithium compounds (RLCs) on the surface,[28,29] unstable cathode–electrolyte interphase (CEI),[30–32] and growth of micro-cracks.[33,34] Therefore, operating a battery at high voltages causes side reactions and structural collapse leading to severe capacity fading and safety risk.[22,35] Similar to the anode solid electrolyte interphase (SEI), modeled by Peled *et al.*,[36] the CEI forms spontaneously upon contact with the electrolyte, and its composition and structure can change during the charge/discharge process.

Various strategies have been proposed to mitigate these degradation mechanisms, with many focusing on controlling cathode–electrolyte interface chemistry. Approaches such as morphology tailoring, elemental doping, coating, core–shell and gradient-concentration structures, and electrolyte modification with additives have been explored.[37–39] Among these, surface modification has proven to be a simple and effective strategy. Coating, in particular, is considered an important method for stabilizing cathodes during long-term cycling and enhancing performance.[40] Various coating materials, including metal oxides,[41–43] fluorides,[44–46] phosphates,[47–49] ionic conductors,[50–52] polymers,[53,54] and different electrode materials,[55,56] have been shown to improve cathode performance. The effectiveness of the protective layer depends on the suitability of the coating material for the cathode, its chemical stability within the operating voltage range, its integrity and uniformity, and its thickness to allow for proper Li^+ diffusion and electron transfer.[57–60]

While research has mainly focused on coating cathode active material (CAM) particles, applying a coating layer on top of the cathode surface has also been explored.[61–63] Among methods for creating thin layer coating, gas-phase

School of Chemistry, Tel Aviv University, Tel Aviv 6997801, Israel.
E-mail: golod@tauex.tau.ac.il

† Electronic supplementary information (ESI) available: See DOI: https://doi.org/10.1039/d4lf00319e

deposition techniques such as atomic layer deposition (ALD) and chemical vapor deposition (CVD) are commonly used due to their precise angstrom-level control, which enables the construction of conformal, pin-hole free layers without using solvents. However, these methods are expensive, involve complex equipment, high temperatures, and precursors that require special handling, and are characterized by low yield and long operation times. Moreover, these techniques may not be compatible with all ceramics due to specific process requirements.[64,65] Conversely, liquid-phase thin-film coating techniques, including spray-, dip-, spin-, and drop-coating, offer a cost-effective and versatile alternative, though achieving consistent thickness control (from nanometers to micrometers) and uniformity, especially for ceramic coatings, remains challenging.[66,67]

In this study, we present the development of a high-performance composite artificial CEI using the electrophoretic deposition (EPD) method.[68] In EPD, suspended charged particles, along with their lyosphere (counterions surrounding the particle), migrate under an applied electric field towards an oppositely charged electrode (electrophoresis). This is followed by the thinning of the lyosphere in the vicinity of the electrode and film formation.[69–71] Our research is the first to use EPD for creating an artificial CEI (ART-CEI). EPD is a fast and simple approach that produces thin and uniform layers with good adhesion to the electrode surface. The thickness and composition of the resulting coatings at the micron scale can be controlled by straightforward adjustments to process parameters.[71–74]

Inasmuch as suspended particles have a small surface charge, additional charging agents, like polyelectrolytes, are used to facilitate migration and produce thin ceramic films in EPD. These polyelectrolytes adsorb onto the particle surface, integrate into the films, and act as binders.[72,73] Herein we introduce the use of a polymerized ionic liquid (PIL), PDMS-*g*-MPA·Li^+_{13}/$PEGMEMA_{27}$,[75,76] as a charging agent for ceramic particle deposition on a commercial $LiNi_{0.6}Mn_{0.2}Co_{0.2}O_2$ cathode (NMC622), as shown in the schematic illustration of the process in Fig. 1. PILs are essentially single-ion conductors in which the counterion is attached to the polymer chain, known for their stability at high operating voltages in electrochemical devices.[77] In the EPD coating of the NMC, the PIL was used as a binder for Li_6PS_5Cl (LPSC) nanoparticles, ion-conductive ceramics from the argyrodite family. LPSC is a low-cost material prepared by a simple synthesis with high ionic conductivity ($\sigma \approx 2.0 \times 10^{-3}$ S cm^{-1} at room temperature).[78,79] It was found that despite the relatively low electrochemical stability of LPSC, its reversible redox processes may contribute to capacity retention,[80–82] as reported in all-solid-state batteries with $LiNi_{0.85}Mn_{0.05}Co_{0.1}$ cathodes, where a sulfide-based ART-CEI was formed *via* a dry-coating approach.[83] The thin composite coating deposited on the high-voltage cathode is expected to create an artificial interphase between the NMC cathode and the electrolyte, suppressing side reactions of the electrolyte, stabilizing the CEI layer, enhancing Li-ion diffusion, and ultimately improving cathode performance.[40,60]

Experimental

Coating technique by EPD

The Li_6PS_5Cl (LPSC)-based coating, synthesized by Zitoun's research group, was deposited on a $LiNi_{0.6}Mn_{0.2}Co_{0.2}O_2$ (NMC622, NEI Corporation, CAM loading: 11.4 ± 0.06 mg cm^{-2}, 2.0 ± 0.1 mA h cm^{-2}) cathode sheet by an anodic EPD process. The polymerized ionic liquid (PIL), a grafted copolymer of poly(dimethylsiloxane)–poly(lithium-1-[3-(methacryloyloxy)propylsulfonyl]-1-(trifluoromethanesulfonyl) imide/poly(ethylene glycol methyl ether methacrylate) (PDMS-*g*-MPA·Li^+_{13}/$PEGMEMA_{27}$),[71,72] was utilized as a charging agent in the deposition process and a binder in the resulting deposited coating. The PIL was synthesized by Sokolov's research group.[71,72] The EPD bath was based on extra-dry acetonitrile solvent (AcroSeal™, Thermo Scientific Chemicals), and the entire protocol was conducted in a glovebox under an argon environment. The suspension contained LPSC and PIL in a ratio of 67 : 33 (W/W%), and 0.6% (W/V) TritonX-100 (Sigma Aldrich), with a total solid loading of 1.3 mg ml^{-1}. Prior to the EPD process, the suspension was homogenized. A Keithley source meter (model 2400), interfaced with LabTracer software, was used to control the EPD process and monitor the current and

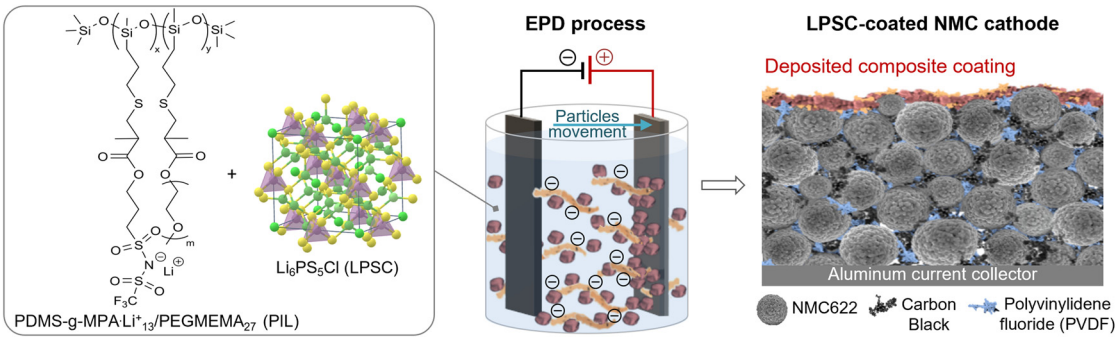

Fig. 1 Schematic illustration of the EPD process and the resulting LPSC-coated NMC622 cathode.

voltage profiles. A constant voltage in the range of 50–125 V was applied between the NMC622 cathode sheet and the glassy-carbon electrode inside the EPD suspension. After coating, the LPSC-coated NMC samples were cut into 12 mm diameter circular discs and dried overnight under vacuum at 100 °C. Finally, the cut cathodes were transferred and stored in an argon-filled glovebox with less than 10 ppm water and oxygen.

Characterization of the cathodes

The structural characterization of pristine and LPSC-coated cathodes was performed by X-ray diffraction (XRD, Bruker D8 Discover) analysis. XRD patterns were recorded using Cu Kα radiation over a 2θ range of 10° to 80° and a step size of approximately 0.02°. These measurements were conducted by transferring the samples under an argon atmosphere in a specialized vessel to avoid ambient air exposure. Surface morphology was analyzed using a high-resolution field emission scanning electron microscope (HRSEM, Zeiss GeminiSEM 300). Energy-dispersive X-ray spectroscopy (EDX) measurements were taken with a Bruker X-Flash 6/60 detector and processed *via* ESPRIT software. Cross-section HRSEM images of the coated cathode were obtained for thickness measurements using a focused ion beam (Ga) and a scanning electron beam (Helios 5 UC DualBeam, Thermo Scientific™) following carbon coating. Coating porosity percentages were estimated from HRSEM images using ImageJ software. Time-of-flight secondary ion mass spectrometry (TOF-SIMS) analysis was performed on the coated cathode, with sample transferred under an inert gas environment to the Physical Electronics device (TRIFT97). X-ray photoelectron spectroscopy (XPS) measurements were conducted on pristine LPSC ceramic powder, pristine PIL, and LPSC-coated cathode samples. Samples were mounted under argon and transferred to the analysis device without air exposure. XPS tests were performed using a Thermo Scientific™ ESCALAB™ QXi XPS Microprobe, with an Al Kα excitation source, spot diameters of 200 μm for the PIL sample and 650 μm for the others, and a resolution of 0.1 eV. The carbon 1s peak at 284.8 eV was used as an energy reference. Raman spectra were recorded at room temperature using a Raman spectrometer consisting of a 532 nm laser (BWN-532-20E, B&W Tek), an optical microscope (BXFM-F and BMXFM-ILHS, Olympus), and a CCD camera (U-DP, Olympus). The beam was focused to a diameter of 1 μm using a 100× objective (M Plan Apo). Raman spectra were collected with a grating of 1800 grooves per millimeter and an acquisition time of 60 seconds from five different locations on the NMC samples. Analysis of cycled electrodes was performed after they were washed in dimethyl carbonate (DMC) solvent to remove excess salt and dried in a vacuum.

Cell assembly and electrochemical characterization

The cells were assembled in CR2032 coin cell compartment in an argon-filled glovebox with a NMC622 cathode (ø 12 mm), a Li metal electrode (MSE Supplies, ø 15.6 mm), a Celgard® 2400 separator, and 60 μl of a commercial electrolyte containing 0.95 M lithium hexafluorophosphate ($LiPF_6$) and 0.05 M lithium bis(oxalato)borate (LiBOB) in ethyl methyl carbonate (EMC) : dimethyl carbonate (DMC) : fluoroethylene carbonate (FEC) : propylene carbonate (PC) 3 : 3 : 3 : 1 (E-Lyte innovations). All electrochemical examinations were carried out at 30 °C. Electrochemical impedance spectroscopy (EIS) measurements were performed using a BioLogic VMP3 potentiostat over a frequency range of 1 MHz to 10 mHz with a 20 mV amplitude. The resistances (R [Ω]), capacitance (C [F]), and Warburg impedance (W [Ω $s^{-0.5}$]) were estimated using the BioLogic Zfit tool. Additionally, distribution of relaxation time (DRT) calculations were conducted with Python-based DRTtools (pyDRTtools).[84,85] Galvanostatic cycling was carried out from 2.8 V to 4.3 V and 4.5 V cutoff voltages *versus* Li^+/Li using a BioLogic BSC-800 battery cycler. Before cycling at charge–discharge rates of 0.5–1.0C, the cells underwent activation through three cycles at rates of C/15–C/15 in a CCCV charge profile, holding the cells in a charged state for 3 hours. For C-rate tests, the charge–discharge rates were varied every ten cycles from 0.1–0.1 to 0.2–0.2, 0.5–0.5, 0.5–1.0, 0.5–2.0, and 0.5–5.0C. Subsequently, the cell was cycled again for ten cycles at 0.1–0.1C, followed by 30 cycles at 0.5–1.0C.

Results and discussion

Creating LPSC coatings on the NMC622 cathode *via* the EPD method

Since the PIL is an anionic polymer, it was used as a charging agent for suspended argyrodite particles, enabling an anodic EPD process to form the composite coating on the NMC622 cathode (Fig. 1). The influence of the coating on the electrochemical performance of the cathode depends, among other factors, on the uniformity of the layer and its low thickness. These aspects are essential to providing effective protection while allowing lithium ion diffusion/migration.[40] Therefore, various EPD process parameters were tested to determine the relationship of the applied voltage and deposition time to the resulting deposited mass (Fig. 2). The results indicated a nearly linear increase in the mass of the deposit with applied voltage. The initial examination showed

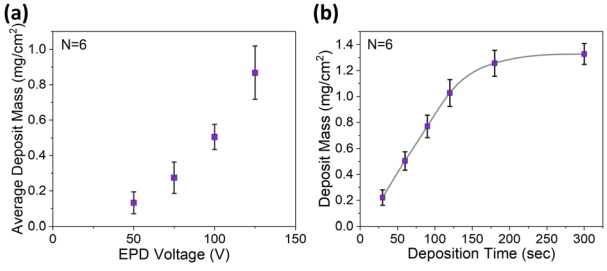

Fig. 2 (a) Average deposit mass for 1 min at different applied voltages, and (b) the deposit mass EPD rate at 100 V of LPSC + PIL on NMC622 cathode.

that the most uniform coatings were obtained at a voltage of 100 V. A linear five-fold mass growth of the LPSC-based composite was observed as the EPD time increased from 30 to 120 sec, followed by a plateau at durations exceeding 150 sec. All further electrochemical tests described below were conducted on NMC622 cathodes coated with an LPSC-based composite that also contained the PIL polymer, deposited at 100 V for 60 s.

Structural and surface characterization of the cathodes

The morphology of the cathodes was characterized using high-resolution scanning electron microscopy (HRSEM) (Fig. 3a). At low magnification, both pristine and LPSC-coated cathodes displayed similar morphology. High-magnification images revealed a thin coating layer conformally covering the spherical secondary CAM particles. Cross-sectional images indicated that the composite coating varied in thickness (Fig. 3b), ranging from 0.5 to 2.2 micrometers, with an average thickness of 1.78 ± 0.52 μm (N = 30). Additionally, the coating displayed ~32% porosity while maintaining good adhesion to the cathode's complex surface.

Element mapping using energy-dispersive X-ray spectroscopy (EDS) confirmed a homogeneous element distribution within the composite (Fig. 3c), and further indicated that the coating contained about 0.99 wt% of PIL. Time-of-flight secondary ion mass spectrometry (TOF-SIMS) chemical imaging and depth profiling validated uniform coverage across the cathode surface, with a consistent LPSC : PIL ratio (represented by the S : Si atomic ratio) throughout the depth profiling (Fig. S1, ESI†).

X-ray photoelectron spectroscopy (XPS) measurements of the LPSC ceramic powder and the LPSC-coated NMC cathode indicate that the pristine LPSC powder was partially oxidized and underwent further oxidation upon deposition (Fig. 4a).[80,86] The S 2p spectrum of the pristine powder showed a main S $2p_{3/2}$ doublet at a binding energy (BE) of 161.6 eV, attributed to the sulfur atom in PS_4^{3-} argyrodite structure (red component). Another weak component at 167.0 eV is explained by traces of sulfite (SO_3^{2-}), likely due to partial sulfur oxidation (brown component). This oxidation occurred despite thorough processing in an argon-filled glovebox. Two additional spectral features appear in the LPSC coating at BEs of 162.3 and 163.5 eV (blue and green components respectively), consistent with the presence of lithium polysulfide (Li_2S_n) and phosphorus sulfide (P_2S_x) species, which are oxidation products of argyrodite. These components belong to the lithium thiophosphate Li_2S–P_2S_5 binary system (LPS), a sulfide glass-ceramic electrolyte, whose conductivity depends on the component ratio and synthesis process.[87] Our experimental data aligns with the initial oxidation of argyrodite in cells,

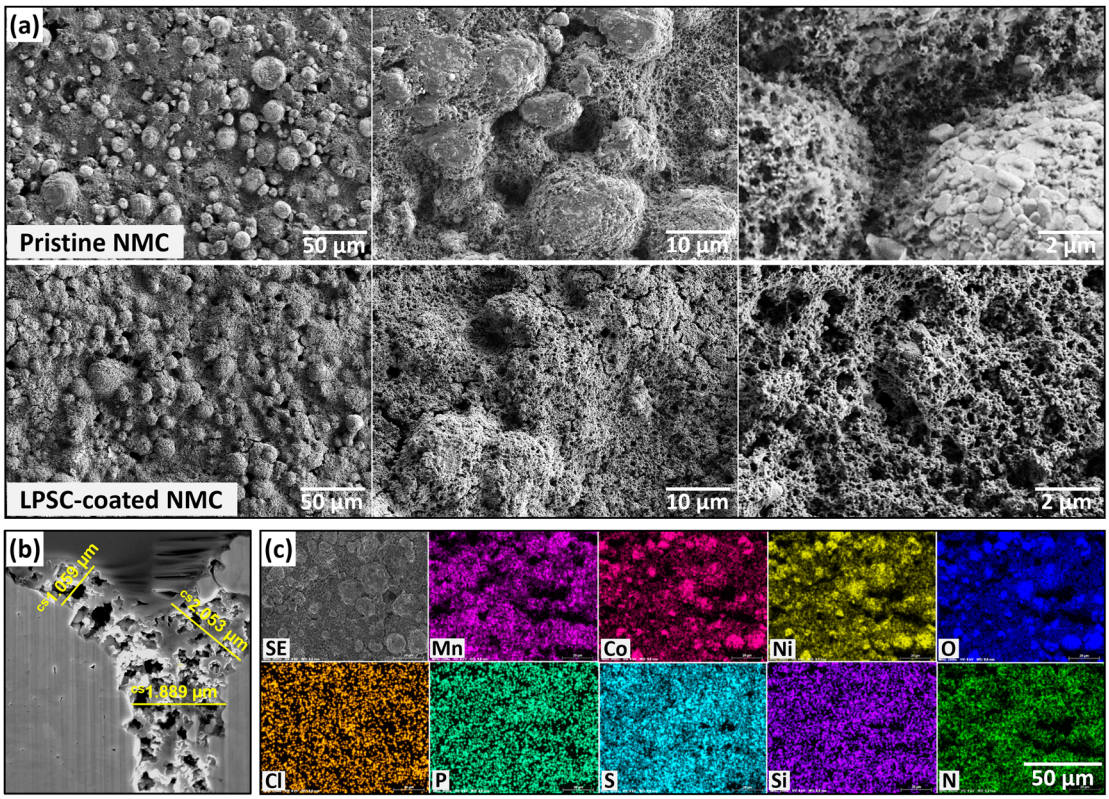

Fig. 3 (a) HRSEM images of pristine and LPSC-coated NMC622 after deposition at 100 V for 1 min. (b) FIB-HRSEM cross-sectional image of the LPSC + PIL coating layer over the NMC particles. (c) HRSEM and EDS mapping images of LPSC film electrophoretically deposited on NMC622 at 100 V for 1 min.

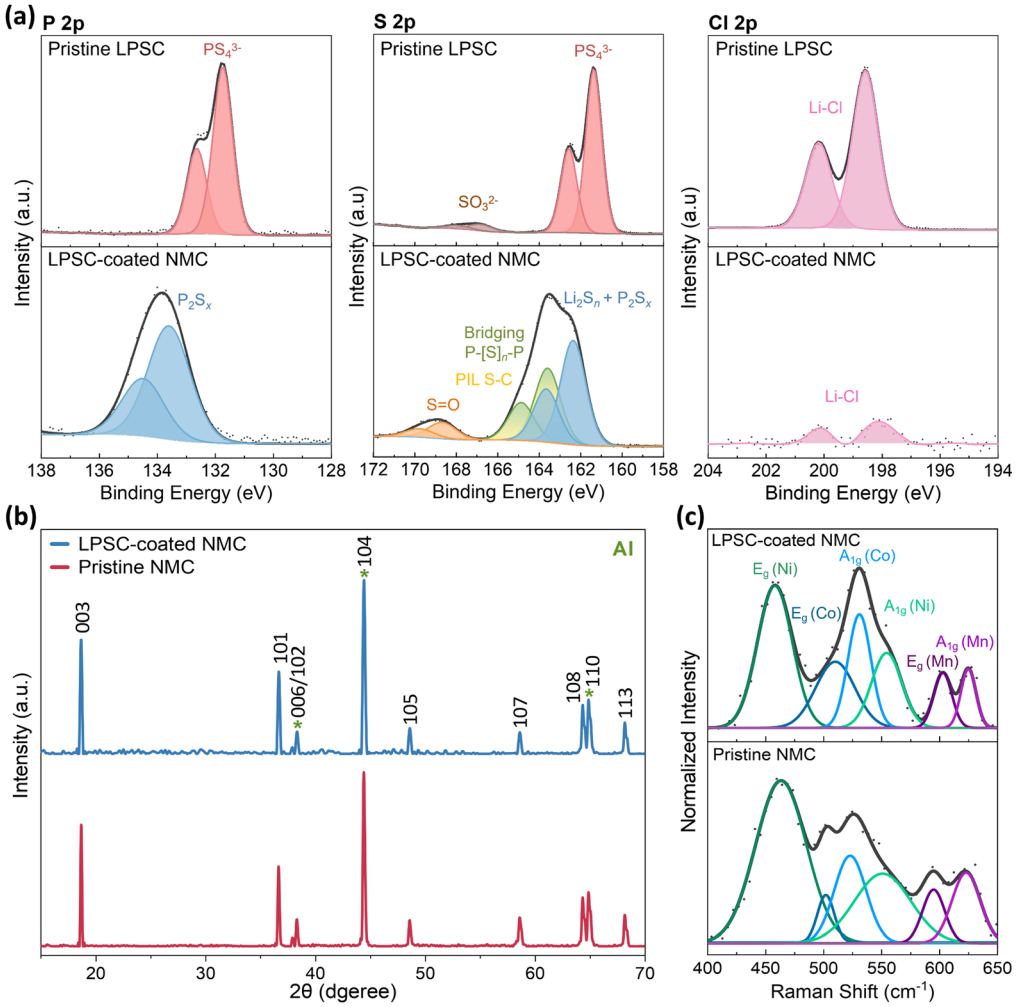

Fig. 4 (a) P 2p, S 2p, and Cl 2p XPS spectra of pristine LPSC powder and LPSC-coated NMC622. (b) XRD patterns and (c) Raman spectra of pristine and LPSC-coated NMC622 cathodes.

which forms a mixed thiophosphate, LPS-like phase that undergoes a reversible redox reaction.[80,82] This is consistent with findings from the wet chemistry synthesis of LPS in acetonitrile, where it was observed that an annealing-less synthesis process produces an amorphous solid electrolyte with a room temperature conductivity of 1.6×10^{-4} S cm^{-1}.[87–89] In the coating, XPS signatures of terminal sulfur (P═S groups, in blue) and bridging sulfur (P–[S]$_n$–P groups, in green) were associated with lithium thiophosphate. The intensity of the bridging peaks was higher than expected relative to the terminal sulfur, likely due to the overlap with PIL peaks at 163.3 and 164.5 eV (C–S–C groups, in yellow), which could not be distinguished and separated (see the S 2p spectrum of the PIL in Fig. S2†). Likewise, the sulfoxide group (S═O, orange) at BEs of 168.6 and 169.6 eV may be associated with both the PIL and a high oxidation state of sulfate (SO_4^{2-}, 169.3 eV). The P 2p spectra showed a characteristic bond of pristine argyrodite as a $2p_{3/2}$ doublet at a BE of 131.8 eV (red component). In the coating, the doublet at a BE of 133.5 eV (blue component) corresponded with the XPS signature of P_2S_x and the S 2p spectrum. In addition, oxidation led to the release of lithium chloride, soluble in acetonitrile, and thus the intensity of the Cl 2p peak in the coating is relatively low. The calculated PIL content in the coating was 1.2% wt, matching the EDS analysis results.

X-ray diffraction (XRD) patterns of pristine and LPSC-coated NMC622 cathodes, along with the corresponding Miller indices (*hkl*) for the peak planes, are presented in Fig. 4b. These patterns reveal characteristic reflections of the NMC622 hexagonal space group $R\bar{3}m$ (powder diffraction file 66-0854).[90] The splitting of the (006)/(102) and (108)/(110) peaks, indicative of the layered phase, was clearly distinguished, and no additional NMC phases were observed during the EPD process. Hence, the structural stability of the active NMC material and integrity of the cathode were preserved after the EPD process, and an amorphous LPS coating formed, as agreed with XPS analysis. To determine the lattice parameters *a* and *c*, the hexagonal *d*-spacing formula for the $R\bar{3}m$ crystal structure was used (eqn (1)), applying the Miller indices and interplanar spacing (d_{hkl}) derived from Bragg's Law (eqn (2)). In this equation, *n*

represents the diffraction order (typically 1), λ is the X-ray wavelength (Cu Kα 1.5418 Å), and θ is the Bragg angle.[91]

$$\frac{1}{d_{hkl}{}^2} = \frac{4}{3}\cdot\frac{h^2+hk+k^2}{a^2} + \frac{l^2}{c^2} \quad (1)$$

$$d_{hkl} = \frac{n\lambda}{2\sin\theta} \quad (2)$$

The calculated lattice parameters of the pristine and LPSC-coated cathodes indicated negligible changes in cell parameters (Table 1), although the c/a value increased slightly following the coating. The lattice parameter c represents the sum of the slab and interslab space thickness in the layered cell unit, where a larger c value is generally correlated with improved diffusion within the cathode lattice and faster Li-ion insertion/extraction.[92,93]

The structure of the NMC622 cathodes was investigated by Raman spectroscopy as a complementary tool to substantiate the XRD results. Fig. 4c compares the deconvoluted Raman spectra of pristine and LPSC coated cathodes in the 400–650 cm^{-1} range, where the active modes are observed.[94–96] Each transition metal ion has two Raman modes: A_{1g} and E_g, associated with M–O symmetrical stretching and M–O–M bending mode vibrations, respectively. The positions of the bands in both the pristine and coated cathodes correspond well to the reported bands of the NMC layered structure (Table 2). An analysis of the Ni modes, the metal with the highest concentration, reveals negligible shift in the peak positions of A_{1g} (Ni) and E_g (Ni) between the samples. The normalized band intensity for both samples was also similar, with a difference of less than 10%, indicating that the Ni^{2+}/Li^+ cation mixing did not change because of the EPD process. In terms of the peak width (FWHM), the pristine cathode exhibited broader A_{1g} (Ni) and E_g (Ni) bands, implying shorter phonon lifetimes. This phenomenon was also observed in other A_{1g} modes, in which oxygen atoms vibrate in a symmetrical stretch parallel to the c axis. The sharpness of the peaks in the coated cathode suggests more stable vibrational modes, as the energy levels are better defined and there is less broadening due to scattering processes. These results are consistent with the structural analysis from XRD, which showed an increase in the c/a cell parameter ratio in the coated cathode. A possible reason for this could be O-site doping by electronegative elements, such as chlorine or sulfur, which increases the interlayer electrostatic repulsion.[97–99] This results in an expanded c cell parameter, potentially improving cathode performance as discussed below.

Table 1 Lattice parameters of the pristine and LPSC-coated NMC622 cathodes

Cell parameters	a [Å]	c [Å]	c/a [Å]	V [Å^3]
Pristine NMC	2.8708	14.2381	4.9596	101.6242
LPSC-coated NMC	2.8694	14.2419	4.9634	101.5849

EIS analysis of symmetrical NMC/NMC cells

The ionic conductivity of the EPD composite coating was evaluated by electrochemical impedance spectroscopy (EIS). The data are presented as Nyquist plots, including their fit to equivalent circuit analogs (Fig. 5). The spectra of symmetrical NMC/NMC cells consist of one suppressed semicircle, which was fitted according to the equivalent circuit scheme shown in Fig. 5a. The broad semicircle, which can be fitted to the first group of RC elements, includes contributions from the resistance of the electrode's surface films (R_{SF}) attributed to the cathode–electrolyte interphase layers, namely, native and ART-CEI, and the corresponding constant phase element (Q_{SF}). The second semicircle in the low-frequency RC domain reflects the charge transfer resistance of electrochemical reactions (R_{CT}) and the corresponding constant phase element (Q_{CT}). Additionally, the high-frequency resistance, bulk resistance (R_{Bulk}), is assigned to the ohmic resistance of the electrolyte, and the Warburg impedance (W) in the low-frequency range reflects lithium diffusion in the electrodes and electrolyte.[100] Since the diffusion of ions is much faster in the liquid electrolyte than in the solid electrodes, the major contribution to Warburg resistance comes from the latter.

The EIS data of symmetric cells assembled with two pristine or LPSC-coated cathodes and the table of calculated equivalent fit values are shown in Fig. 5b and Table 3. The conductivity of the coating on the cathode was estimated by using eqn (3):

$$\sigma_{coating} = \frac{2l_{coating}}{\left(R_{SF(coated)} - R_{SF(pristine)}\right)A} \quad (3)$$

where $l_{coating}$ is the coating thickness, A is the cathode area, and $R_{SF(coated)}$ and $R_{SF(pristine)}$ are the fitted surface film resistances of the corresponding symmetric cells. Based on the difference between the R_{SF} of the coated and pristine cathodes, the conductivity of the artificial CEI was calculated to be 0.12 mS cm^{-1} at 30 °C, corresponding to the reported conductivity of amorphous LPS.[88]

Electrochemical performance of NMC/Li half cells

The voltage profiles of the first two cycles at a C/15 rate and the corresponding differential capacity *versus* voltage plots of NMC/Li cells comprising pristine and LPSC-coated NMC622 cathodes are presented in Fig. 6. The electrochemical reactions during charging, from open circuit voltage (OCV) to 4.5 V, showed a slight difference in the trend of the curves. Starting at ~3.7 V, the plateaus are related to the oxidation of nickel and cobalt (Ni^{2+}/Ni^{4+}, and Co^{3+}/Co^{4+}) with the extraction of Li-ions from the NMC. This process causes phase transformations from the $Li(TM)O_2$ hexagonal (H1) phase to the monoclinic phase (M), then to another hexagonal phase (H2), and finally to the hexagonal phase (H3).[11,12] The sharp dQ/dV peak in the first delithiation process at about 3.7 V is associated with the H1–M phase transition (Fig. 6a and b). Here, the cell with the coated cathode displays a shift to a higher potential with an increase

Table 2 The parameters of the six fitted Raman spectra bands for the pristine and LPSC-coated NMC622 cathodes

Band	Mode	Band position (cm^{-1})		FWHM (cm^{-1})	
		Pristine NMC	LPSC-coated NMC	Pristine NMC	LPSC-coated NMC
ν_1	E_g (Ni)	461	458	52	35
ν_2	E_g (Co)	503	511	17	40
ν_3	A_{1g} (Co)	524	531	33	24
ν_4	A_{1g} (Ni)	551	554	57	31
ν_5	E_g (Mn)	596	603	23	18
ν_6	A_{1g} (Mn)	623	625	29	15

in overpotential (by 50 mV) compared to the pristine cell, possibly due to a non-uniform coating layer. During consequent cycles, the oxidation peaks become more prominent (Fig. 6c and d). The sharp peak that appeared as two overlapping peaks during the first cycle is separated into two peaks: one for the transition from the H1 phase to a mixed state of M and H1, and another for the transition from the mixed state to the M phase. Additionally, the profiles show no shifts in the reduction processes following the coating, but an additional peak appeared at 3.46 V, which is more prominent in the second cycle. Furthermore, the cells with the coated cathode demonstrate higher discharge capacity values by 8–14 mA h g^{-1} compared to the pristine cells in the two activation cycles at a C/15 rate and cutoff voltage of 4.3 V and 4.5 V (Table S1, ESI†). Also, the first two cycles showed similar coulombic efficiency (CE) for both the pristine and coated cathodes, with ≈92% and ≈99% in the first and second cycles, respectively.

A long-term cycling study at charge–discharge rates of 0.5–1.0C was performed at cutoff voltages of 4.3 V and 4.5 V after three activation cycles at a C/15 rate (Fig. 7a and b). In the first cycle at a 1.0C discharge rate (4th cycle), discharge capacity values of 162 mA h g^{-1} and 164 mA h g^{-1} at 4.3 V, and 186 mA h g^{-1} and 191 mA h g^{-1} at a cutoff voltage of 4.5 V were observed for pristine and LPSC-coated NMC622 cathodes, respectively. After 200 cycles, the LPSC-coated cathode provided significantly improved discharge capacity values and exhibited higher capacity retentions of 148 mA h g^{-1} (90%) and 159 mA h g^{-1} (83%) compared to 129 mA h g^{-1} (80%) and 136 mA h g^{-1} (73%) for the pristine cathode, at cutoff voltages of 4.3 V and 4.5 V, respectively.

Fig. S3† and 7c and d show the average voltage and voltage hysteresis profiles for half-cells comprising pristine and LPSC-coated NMC622 cathodes at cutoff voltages of 4.3 V and 4.5 V. The voltage gap between charge and discharge shows that, while average charge voltages remain similar between the pristine and coated cathodes, after 200 cycles, the LPSC-coated cathode's average discharge voltage is 80 mV higher. This suggests that Li^+ insertion into the pristine cathode is impeded, as reflected in the increasing potential gap, which is directly proportional to the internal resistance of the electrodes.[101,102] The latter depends on the kinetics of redox processes, the activation energy of lithium insertion/extraction, and diffusion complicated by phase transitions. Voltage hysteresis, estimated by the voltage difference between charge and discharge curves at half capacities, increased with cycling. This may be due to degradation of the high-voltage cathode, a significant drawback that reduces battery efficiency and raises safety concerns.[103–105] At a cutoff voltage of 4.3 V, the difference in hysteresis between the pristine and coated cells was not significant over 200 cycles. However, upon charging to a higher potential (4.5 V cutoff), the voltage hysteresis grew, with the LPSC-coated cathode exhibiting a 1.7-fold slower increase in voltage hysteresis (0.753 mV $cycle^{-1}$) compared to the pristine cathode (1.23 mV per cycle). This electrochemical behavior can be attributed to the enhancement of the lithium intercalation/de-intercalation kinetics during cycling owing to the ART-CEI.

Fig. 7e displays the C-rate performance of the cells, demonstrating a preference for the LPSC-coated cathode across all discharge C-rates except at 5C. As shown in the dQ/dV discharge curves in Fig. 7f, increasing C-rates lead to greater cell overpotential due to electrode polarization effects, resulting in lower capacity.[106] The reduced growth of the charge transfer and diffusion resistances in the LPSC-coated

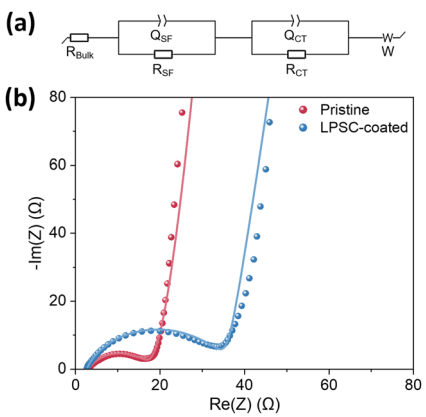

Fig. 5 (a) The equivalent circuit model for fitting the EIS data. (b) Nyquist plots of EIS measurements and their fits at 30 °C of symmetrical cells comprising uncoated and LPSC-coated NMC622 cathodes.

Table 3 Resistances fitted to impedance values of the symmetric cells that comprise NMC622/NMC622 cathodes

	R_{Bulk} [Ω]	R_{SF} [Ω]	R_{CT} [Ω]
Pristine NMC	2.6	3.4	15.9
LPSC-coated NMC	2.6	6.3	32.7

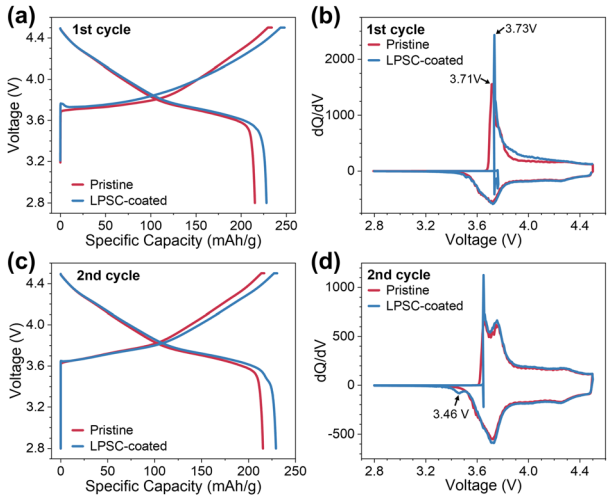

Fig. 6 (a–d) Voltage profiles and corresponding differential capacity *versus V* plots of the pristine and LPSC-coated NMC622 cathodes *versus* Li electrode cells during two consecutive formation cycles between 2.8 and 4.5 V at a cycling rate of C/15.

cathode also improve rate capability. However, as the C-rate increases, polarization at the coated cathode intensifies, narrowing the discharge capacity gap until a sharp drop at 5C. This drop can be explained by a high tortuosity that leads to a diffusion-rate limit at a high C-rate. Still, even at a 5C discharge rate, the coated cathode maintained higher stability and better recovery when the C-rate was reduced, with the capacity difference greater than at the corresponding previous rates.

To better understand the long-term cycling results, a comparison of the voltage profiles and corresponding dQ/dV *versus* V plots for the 5th, 50th, 100th, 150th, and 200th cycles at 4.3 V and 4.5 V cutoff voltages is presented in Fig. S4.† Fig. 8 provides a detailed analysis for the 5th and 50th cycles at a 4.5 V cutoff voltage, including the marking of the accompanied phase transitions (H1 ↔ M ↔ H2 ↔ H3) in the dQ/dV curves.[10,101] The typical H2/H3 transformation peaks that appeared at ~4.3 V indicate anisotropic shrinkage and expansion of the primary CAM particles,

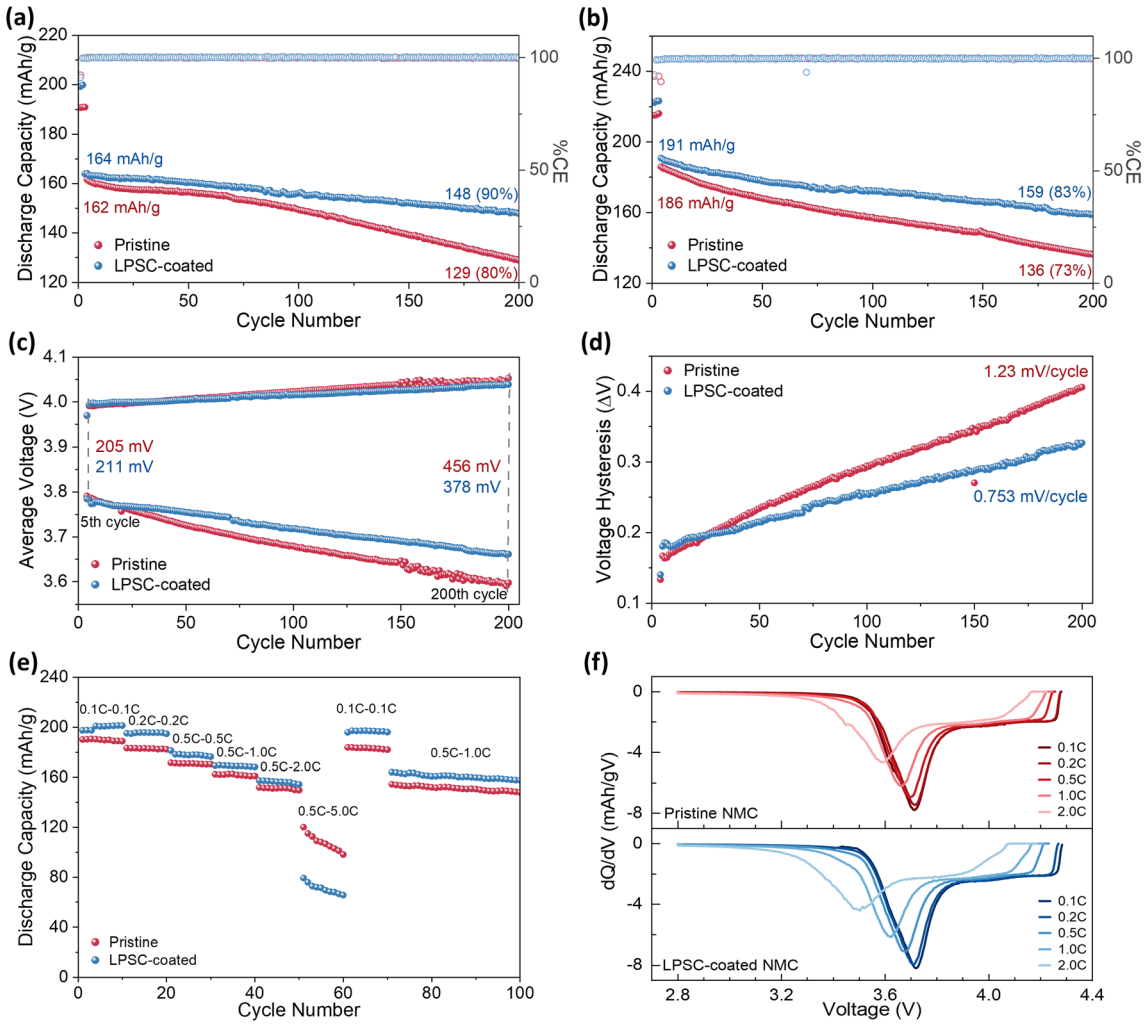

Fig. 7 Long-term electrochemical cycling at 2.8–4.3 V (a), and 2.8–4.5 V (b), for the pristine and LPSC-coated NMC622 cells as indicated at charge–discharge rates of 0.5–1.0C and 30 °C after 3 cycles at C/15. (c) Average voltage profiles on charge and discharge, and (d) voltage hysteresis calculated as the difference between average charge (4.5 V cutoff) and discharge (2.8 V cutoff) voltages. (e) Rate performance at 2.8–4.3 V for the electrodes comprising pristine and LPSC-coated NMC622 as indicated, and (f) the corresponding dQ/dV curves of the 5th cycle discharge at each C-rate.

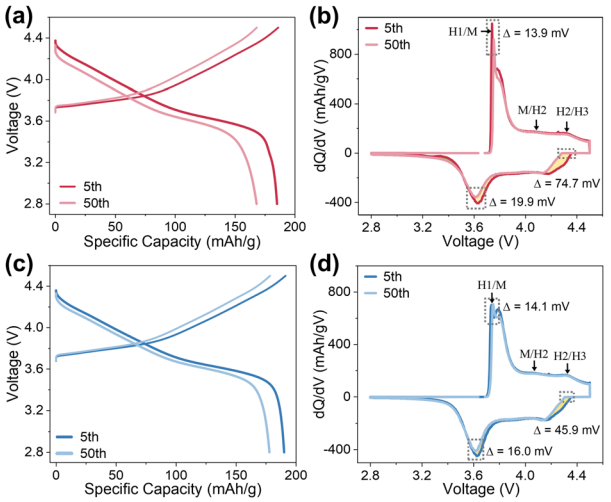

Fig. 8 Voltage profiles and corresponding differential capacity dQ/dV *versus* V plots for half cells comprising: (a and b) pristine and (c and d) LPSC-coated NMC622 cathodes, at cycles number 5th and 50th.

causing intergranular cracks.[34] Hence, this phase transition likely contributes to the capacity retention gap between the examined cutoff voltages (Fig. 7a and b). During cycling, three main polarization regions, marked by squares in the plots (Fig. 8b and d), can be observed.[106] The main oxidation peak of the H1/M phase transition at ~3.7 V is shifted to a higher potential, with no effect of the ART-CEI on the potential shift ($\Delta V \approx 14$ mV) in the first 50 cycles at a 4.5 V cutoff voltage. The sharper peaks of the transition from the H1 phase to a mixed state of M and H1 and from the mixed state to the M phase in the pristine cathode indicate faster phase transformations. In contrast, the discharge peak in the pristine cathode at ~3.6 V shifted to a lower potential, while the shift of the LPSC-coated cathode was slightly lower (ΔV = 16.0 mV compared to 19.9 mV). This significant difference between the cathodes was in the polarization between the end of charging and the beginning of discharging, which increased with prolonged cycling (ΔV = 45.9 mV compared to 74.7 mV). These changes generally indicate an increased internal resistance during cycling, caused by parasitic interfacial side reactions at the cathode–electrolyte interface.[10] Also, the discharge capacity gain (~3.2–3.5 V, marked in green area) was negligible compared to the lost capacity, which was smaller for the coated cathode (~4.2–4.4 V and ~3.6–3.8 V, marked in yellow area). The reduced polarization induced by the coating reflects the observed trend of capacity retention during prolonged cycling, demonstrating improvement at the cathode–electrolyte interface.

Investigation of aging cells by EIS and DRT method

EIS measurements were performed upon cycling, and the fitted resistance values and calculated diffusion coefficients from the Nyquist plots of the 3rd, 50th, 100th, 150th, and 200th cycles at a 4.5 V cutoff voltage are shown in Fig. 9a and b. The differences in the EIS data can be attributed to the ART-CEI. Nyquist plots of these impedance measurements and a summary table of the fitted values corresponding to the equivalent circuit are provided in Fig. S5† and Table S2.† It should be noted that in the third cycle, the values of the Warburg elements and resistances were relatively high, probably due to the incomplete formation of SEI and CEI layers. Therefore, these were excluded from the current comparison but are available in the ESI.†

According to the Nyquist plots (Fig. 9a), after the electrochemical activation of the cells, in which the electrode–electrolyte interphases were formed, starting from the measurement of the 50th cycle, the coating significantly improved the R_{SF} attributed to the SEI and CEI and the R_{CT} reflecting the charge transfer resistance. The R_{Bulk} resistances of the cell with the pristine cathode were slightly lower than those of the LPSC-coated cathode. The observed increase in resistances during prolonged cycling can be attributed to various processes in the cell, such as electrolyte decomposition (increasing R_{Bulk}), SEI and CEI layer growth and decomposition (increasing R_{SF}), and the subsequent slowing of charge transfer reactions (increasing R_{CT}).

The positive effect of the LPSC coating on lithium-ion diffusion is evident from the diffusion coefficients calculated from the Warburg impedance of the EIS measurements (Fig. 9b). The diffusion coefficient (D_{Li}) was estimated from the Warburg element according to the following equation:

$$D_{Li} = \frac{R^2T^2}{2S^2n^4F^4C^2\sigma^2} \quad (4)$$

where R is the gas constant, T is the temperature, S is the surface area of the cathode (0.20 m^2 g^{-1} for the NMC622 commercial sheet), n is the number of electrons involved in the intercalation step, F is the Faraday constant, C is the molar concentration of lithium ions in the cathode, and σ is the fitted Warburg value. These calculations revealed that the diffusion coefficients for the LPSC-coated cathode are twice those of the pristine cathode in all cycles, confirming that the ART-CEI improves lithium-ion diffusion in the electrodes. As expected, the diffusion coefficients for both cathodes decreased with increasing cycle number due to aging of the CAM.[40,60] However, the decline rate of D_{Li} in the protected cathode was 15% lower between the 100th and 200th cycles.

In addition to AC impedance analysis based on the equivalent circuit model, the distribution of relaxation time (DRT) deconvolution method was used to investigate aged cells in the time domain and distinguish between overlapping polarization effects in the frequency domain (Fig. 9c). In the EIS measurements analyzed by DRT, split peaks representing different processes with a typical time constant (τ) are obtained, providing better insights into aging degradation mechanisms.[107–109] The plots in Fig. 9c show the P1 peak at $\tau = 10^{-4}$ s, attributed to electrical and

magnetic effects caused by the contacts between active material particles and the electrodes to current collectors. P2 in the range of $\tau \approx 10^{-3}$ s and P3 in $\tau \approx 10^{-2}$ s correspond to lithium ion migration through the SEI and CEI layers, respectively. The electrodes' charge transfer resistance is observed in the range of $\tau \approx 10^{-2} - 10^{1}$ s, while diffusion processes occur at $\tau > 10^{1}$ s, both appearing as several peaks. The resistances calculated from the DRT analysis peaks align with the fitted values from the Nyquist plots, clearly showing that the coated cathode has lower resistance values. A noticeable difference between the cathodes is seen in the first three peaks (P1, P2, P3). The sum of $R_{contact}$, R_{SEI}, and R_{CEI} values (Fig. 9d) closely matches the fitted R_{SF} resistance excluded from the first semi-circle in the intermediate frequency ranges of the Nyquist plots. Changes in peak intensity and τ are expected during cycling, related to the growth and decomposition of the electrode–electrolyte interphases and the impact of degradation mechanisms such as HF attack, lithium plating, particle cracking, and structural disordering. The coated cathode exhibited less change in τ values of P2 and P3, with a slight shift towards lower time constants compared to the stronger shift to larger τ in the cell with the pristine cathode. DRT analysis reveals that the LPSC-based ART-CEI promotes the stability of the CEI and SEI in the NMC/Li cell. Furthermore, the coated cathode exhibited smaller changes in the $R_{contact}$, R_{SEI}, and R_{CEI} values between 50 and 150 cycles compared to the uncoated cathode. Generally, microcracks in the CAM lead to increased resistance and reduced Li-ion diffusion, eventually resulting in significant cracks that cause a loss of electrochemically active material, followed by a sharp drop in R_{SF} and R_{CT},[95] as shown in the 200th cycle. The formation of an electrochemically inactive material also deteriorates discharge capacity. Thus, the capacity loss of the pristine cathode between 100–150 cycles and 150–200 cycles was 0.17 and 0.26 mA h g^{-1} per cycle,

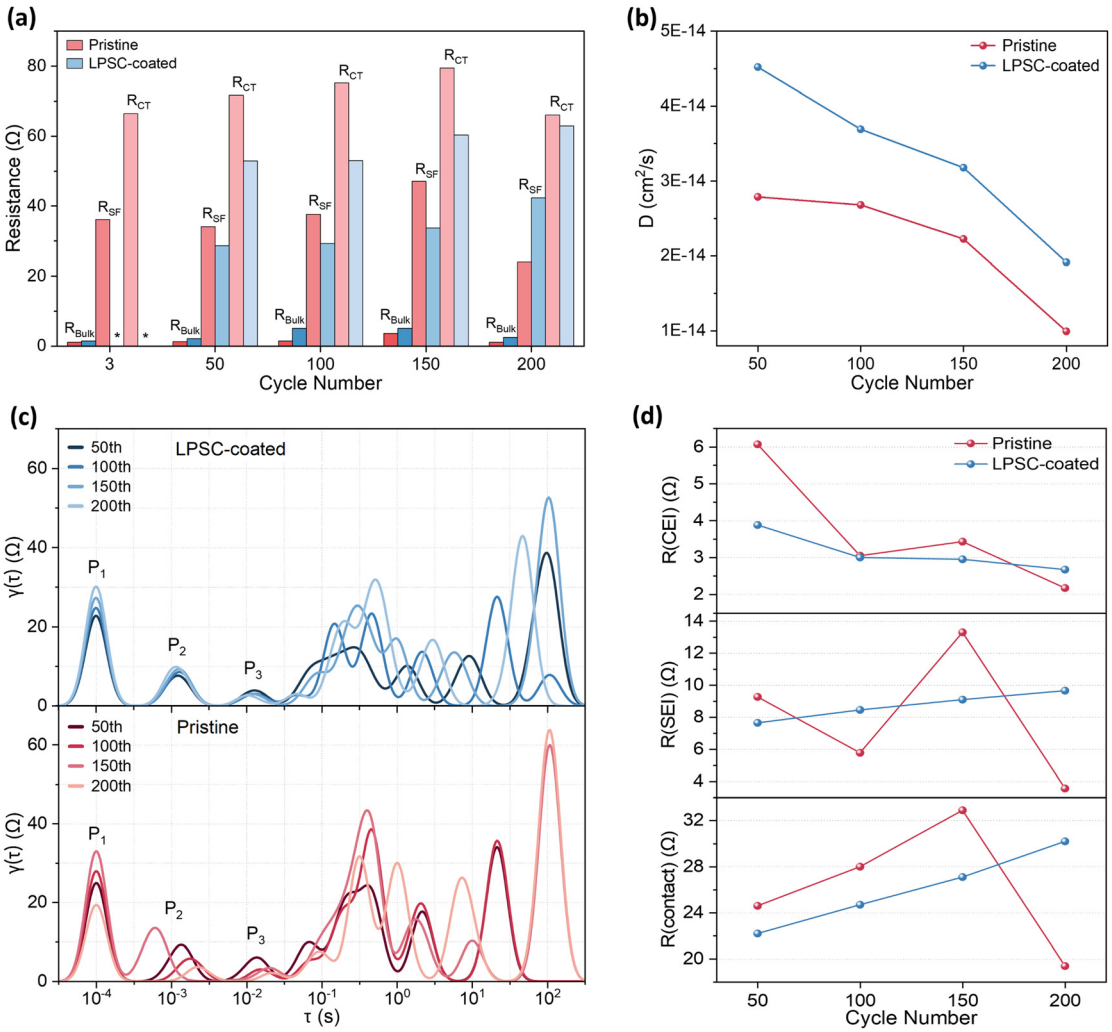

Fig. 9 (a) The fitted resistance values of EIS measurements, (b) the calculated lithium-ion diffusion coefficients, (c) the DRT plots, and (d) the resistances in the intermediate frequency ranges from the DRT plots, during electrochemical cycling after the 50th, 100th, 150th, and 200th cycle at 2.8–4.5 V.

much higher than that of the LPSC-coated cathode, which exhibited losses of 0.12 and 0.14 mA h g^{-1} (Fig. 7b). Overall, the cells' behavior according to EIS is consistent with the long-term capacity loss presented above.

Electrode–electrolyte interphase characterization

To further understand the improved R_{SF} and electrochemical performance of the coated cathode, the electrode–electrolyte interphases were investigated using XPS analysis of the electrodes after 20 cycles. The P 2p, O 1s, Li 1s, and S 2p spectra of the cycled NMC cathodes, along with the atomic concentration in the CEI, are presented in Fig. 10. As shown in Fig. 4a, LPSC decomposes into L_2S–P_2S_5 (LPS) products before cycling. This sulfide glass-ceramic electrolyte was also detected in the CEI of the coated cathode after cycling (S 2p: 162.8 eV; P 2p: 134.8 eV; Li 1s: 58.1 eV). Despite the low sulfur content in the ART-CEI (1.2%), the fraction of sulfur species in the Li 1s spectrum was high, including LPS (44%) and Li_2S (9%) at BEs of 58.1 and 55.0 eV, respectively.[110] Additionally, sulfur species of the SO_x type were observed (O 1s: 532.5 eV; C 1s: 287.4 eV Fig. S6†), which could be associated with the PIL in the coating or other LPSC decomposition products like SO_4^{2-} and SO_3^{2-}. Notably, the lattice metal-oxide bond of the NMC in the O 1s spectrum (528.3 eV) is evident in the pristine cathode but indistinguishable in the coated cathode, suggesting an increased surface layer thickness due to the EPD coating. The higher intensity of the C–C bond at 284.6 eV in the C 1s spectrum of the pristine cathode, related to the carbon black in the cathode, can be attributed to the absence of the coating (Fig. S5†). In addition, peaks assigned to ROLi, CO_3/C═O, C–O, and $ROCO_2R$ species reflect electrolyte solvent decomposition, while the peaks of $Li_xPO_yF_z$ and LiF indicate $LiPF_6$ salt decomposition.[30,31] The O 1s spectrum of the coated cathode contained additional compounds belonging to the coating. However, when cross-referenced with the Li 1s and P 2p spectra, it can be concluded that the ART-CEI contained fewer carbonates (Li_2CO_3/ROCOLi) and $Li_xPO_yF_z$. These findings suggest that the EPD-formed ART-CEI effectively inhibits decomposition reactions at the cathode–electrolyte interface.

The SEI composition on the Li anode in cells with pristine and coated NMC cathodes also differed (Fig. 11). XPS analysis revealed that LPS and PIL components of the coating were presented in the anode SEI as well. The S 2p spectrum indicated that the PIL (164.2 and 168.7 eV) appears in the outer SEI layer of the coated cathode cell, while LPS (162.3 eV) was also observed after sputtering. LPS in SEI is known to facilitate the formation of a homogenous layer, leading to stable lithium plating/stripping.[111–113] The increased sulfur bond intensity in the inner SEI layer was also observed in the binding energy region associated with SO_x species (C 1s: 287.8 eV; O 1s: 532.5 eV), which, apart from the PIL, can be attributed to a high oxidation state of sulfate (SO_4^{2-}, S 2p: 169.3 eV). Additionally, based on the carbon content and deconvoluted C 1s and F 1s spectra, the SEI in the cell with the pristine cathode had a higher concentration of organic species than the coated-cathode cell, especially in the inner layer. In the C 1s spectrum, peaks of C–C/C–H (284.8 eV), C–O (286.7 eV), and C═O (288.8 eV) were attributed to organic components from electrolyte solvent decomposition and polymerization.[114] The intensity of these decomposition

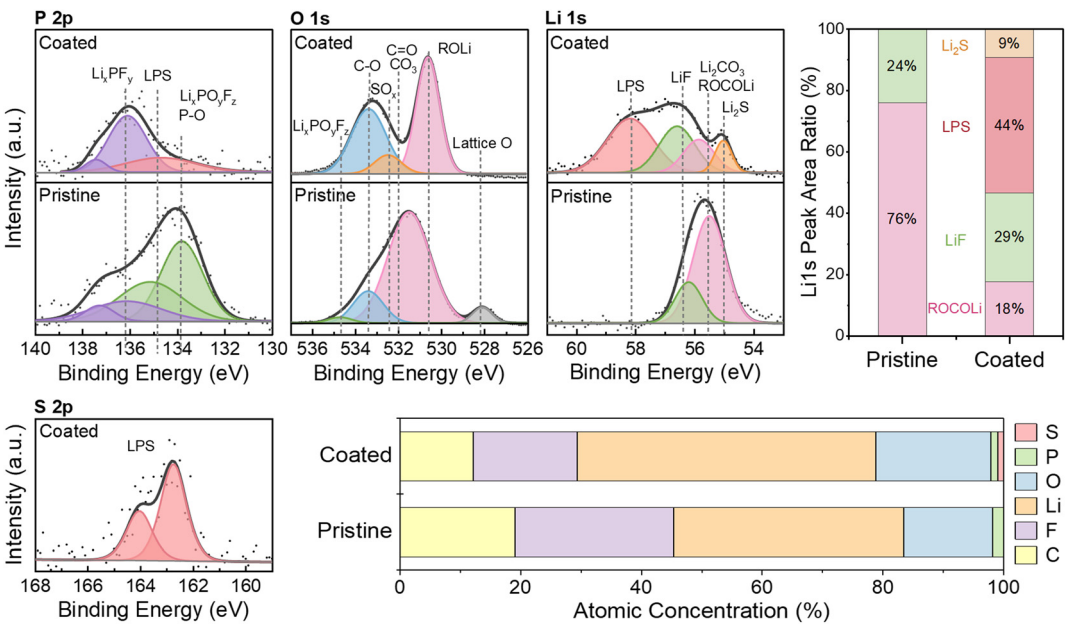

Fig. 10 P 2p, O 1s, Li 1s, and S 2p XPS spectra and the atomic concentrations in the CEI of pristine and LPSC-coated NMC622 after 20 cycles (200 s sputtering); the area ratio of the lithium species components according to the corresponding Li 1s spectra.

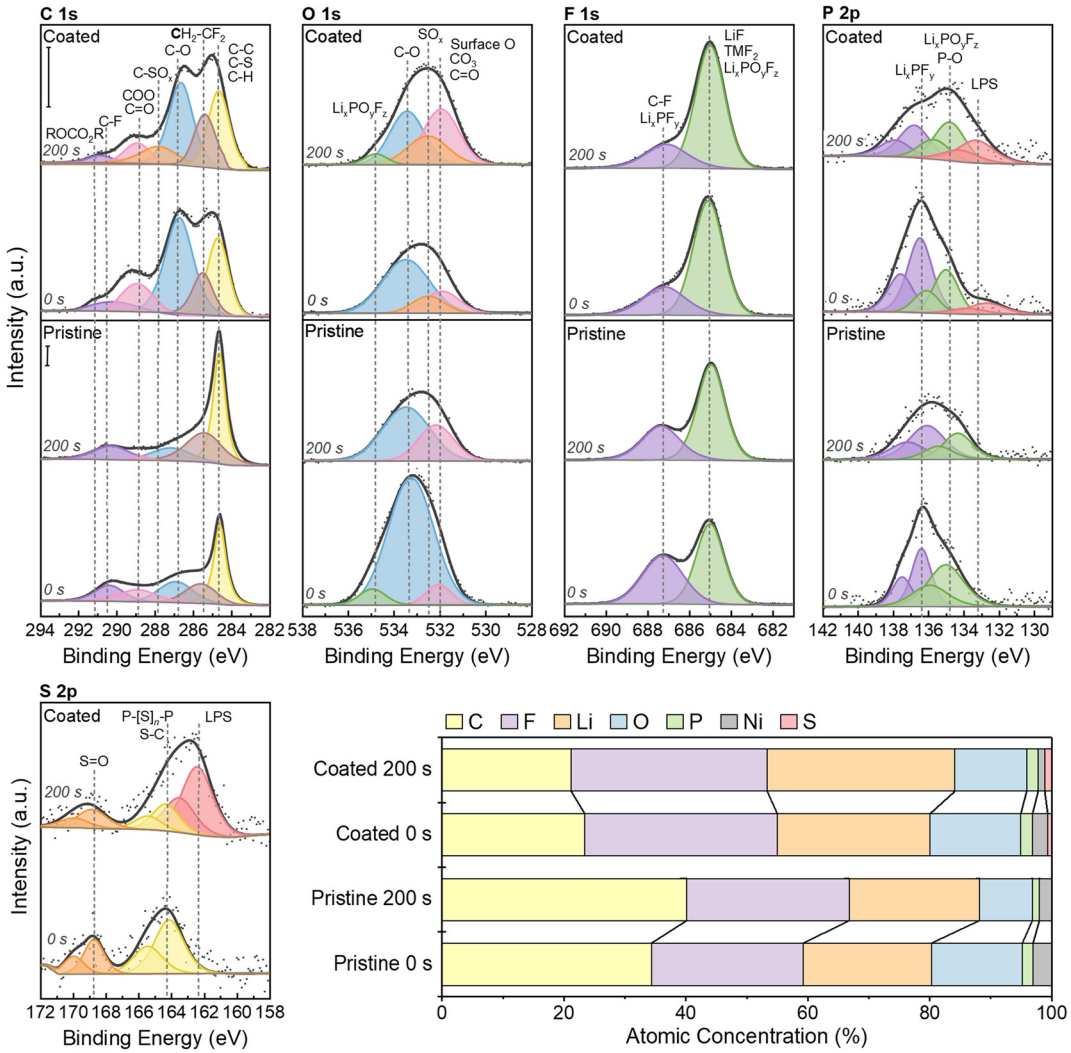

Fig. 11 C 1s, O 1s, F 1s, P 2p, and S 2p XPS spectra and the atomic concentrations in the SEI of Li metal anodes in pristine and LPSC-coated NMC622 cells after 20 cycles (surface and depth profiles after a 200 s sputtering).

product peaks was lower in the coated-cathode cell, as were the overlapping peaks of $ROCO_2R$ (291.3 eV) from fluoroethylene carbonate (FEC) decomposition and C–F (291.6 eV) attributed to polyvinylidene fluoride (PVDF). Furthermore, the decomposition of $LiPF_6$ was confirmed by the presence of LiF and $Li_xPO_yF_z$ peaks (685.1 eV) in the F 1s spectrum. The relatively low content of organic decomposition products and high content of LiF, likely also due to PIL decomposition, suggest the formation of an inorganic-rich SEI in the ART-CEI coated cathode cell. Such inorganic-rich SEI, with a high LiF content, is known to improve Li stripping/plating properties due to its high mechanical strength, leading to a stable SEI, dendrite-free morphology, and high efficiency.[114,115] The Ni 2p spectra showed that the SEI contained metallic Ni and NiF_2 at BEs of 850.1 and 857.8 eV, respectively (Fig. S7†). Transition-metal fluorides (TMF_2), also observed in the F 1s spectrum, are formed through HF attack on the NMC surface, which diffuse into the electrolyte and deposit in the SEI.[30] In addition, the depth profile of the SEI in the ART-CEI coated cell shows the formation of the NiS_x peak, a by-product of LPSC oxidation.[116]

Post-cycling morphological and structural analysis

HRSEM images of the uncoated and LPSC-coated cathodes after cycling reveal a notable morphological difference (Fig. 12a). The pristine cathode exhibited large cracks and partial disconnection of the spherical secondary CAM particles. These observations suggest that although the LPSC coating (also shown in the EDS images in Fig. S8†) was not uniformly maintained after prolonged cycling, the ART-CEI improved the adhesion of CAM particles to the current collector. Hence, the coating, which apparently suppressed parasitic reactions at the NMC/electrolyte interface, also enhanced the mechanical properties of the cathodes. This finding is consistent with electrochemical impedance data showing lower and more stable $R_{contact}$

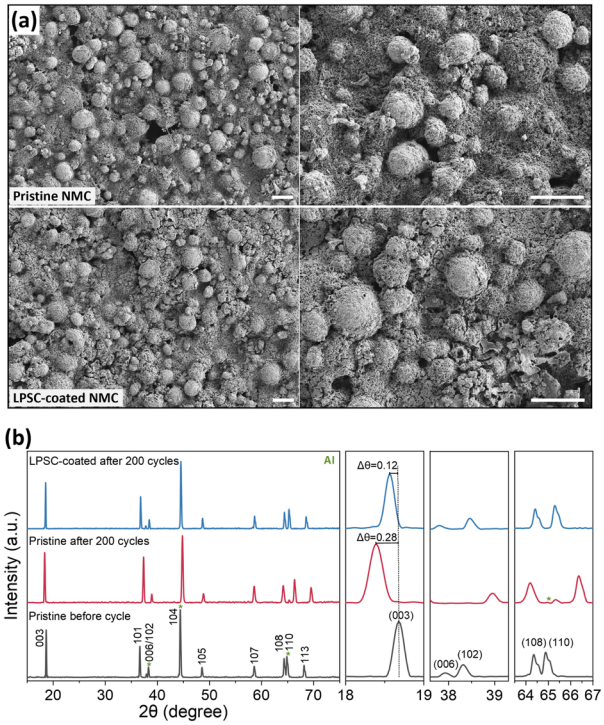

Fig. 12 (a) HRSEM images of pristine and LPSC-coated NMC622 cathode surfaces after 200 cycles, scalebar: 20 μm. (b) XRD patterns of uncycled the pristine NMC622 cathode and pristine and LPSC-coated cathode after 200 cycles, and magnified view of the (003), (006)/(102), and (108)/(110) reflections.

during cycling for the coated cathode compared to the pristine one.

The XRD patterns of pristine and LPSC-coated NMC622 cathodes after cycling, along with magnified regions of the (003), (006)/(102), and (108)/(110) peaks, are shown in Fig. 12b. The (003) peaks shift to a low angle after cycling, indicating expansion along the *c*-axis, as seen in the calculated lattice parameters in Table 4.[90] The cycled pristine cathode exhibited a more pronounced (003) peak shift than the coated cathode compared to the fresh pristine cathode, leading to greater broadening of the *c*-axis. Besides, the (006)/(102) and (108)/(110) peaks corresponding to the layered phase changed in both cathodes after cycling due to the expansion along the *c*-axis, contraction along the *a* and *b* axes, and reduction in unit cell volume.[26,34] As expected, the structural changes were more significant in the pristine cathode, where the (006)/(102) peaks merged into one, and the (108)/(110) peaks split further. The lower changes in lattice parameters (Δa, Δc, and ΔV) after cycling of the coated cathode indicate a higher structural order compared to the pristine NMC cathode. Furthermore, the smaller c/a ratio of the cycled coated cathode indicates a higher Li concentration in the crystal structure and lower mechanical stresses that may lead to lattice distortions and cracks.[34,117] Lattice distortions are also demonstrated by anisotropic peak broadening that significantly affects the (003) reflection. According to the FWHM analysis, the (003) reflection in the XRD pattern of the coated cathode is characterized by a higher crystallite size and lower strain accumulation in the lattice,[117,118] explaining the improved electrochemical properties of the ART-CEI cathode.

Conclusions

In this study, we introduce a facile and fast EPD method to create an ART-CEI, composed of a sulfide electrolyte based on argyrodite (LPSC) and a polymerized ionic liquid, on a commercial NMC622 cathode. The EPD process is easily controlled, allowing precise manipulation of the coating by adjusting the suspension composition, applied voltage, and deposition time. The resulting porous coating adheres well to the cathode surface without requiring an additional calcination step. The amorphous sulfide electrolyte coating significantly enhances the electrochemical performance of NMC/Li cells compared to those with a pristine cathode. LPSC-coated cathode cells exhibit lower R_{SF} and R_{CT} impedance values, along with higher lithium-ion diffusion coefficients during cycling. These improvements lead to stable long-term cycling performance, higher capacity retention, reduced voltage hysteresis, and better rate capability. The cells were cycled for 200 cycles within a voltage range of 2.8–4.5 V, achieving a coulombic efficiency of 99.8% and a capacity loss of only 0.086% per cycle. The performance enhancement is attributed to the suppression of detrimental side reactions at the cathode–electrolyte interface while maintaining efficient diffusion of lithium ions through the ART-CEI. Our findings demonstrate that the sulfide electrolyte coating facilitates the formation of an artificial CEI, enhances the stability of the SEI on the lithium anode, reduces structural disorder in NMC622, mitigates crack formation typically observed during cycling of layered cathodes, and inhibits electrolyte decomposition. Moreover, the EPD coating process is versatile and not limited by the type of deposited particle or substrate, making this surface

Table 4 Lattice parameters of the uncycled pristine and the cycled pristine and LPSC-coated NMC622 cathodes

	a [Å]	c [Å]	V [Å^3]	c/a [Å]	FWHM$_{(003)}$
Pristine NMC before cycling	2.8708	14.2381	101.6242	4.9596	0.146
Pristine NMC after 200 cycles	2.8239 (Δa = 0.0469)	14.4751 (Δc = 0.2370)	99.9621 (ΔV = 1.6621)	5.1259	0.198
LPSC-coated NMC after 200 cycles	2.8606 (Δa = 0.0102)	14.2760 (Δc = 0.0379)	101.1685 (ΔV = 0.4557)	4.9906	0.134

modification technique highly promising for application in high-voltage LIBs.

Data availability

The authors confirm that the data supporting the findings of this study are available within the article and its ESI.†

Conflicts of interest

There are no conflicts to declare.

Acknowledgements

This work was supported by the US–Israel Binational Industrial Research and Development (BIRD) Foundation. The authors express their sincere gratitude to Prof. David Zitoun (Bar Ilan University) and Prof. Alexei P Sokolov (University of Tennessee) for providing essential materials. Acknowledgment is also given to the Tel Aviv University Center for Nanoscience and Nanotechnology for providing instrument access and staff support. Special appreciation goes to Dr Alex Lahav for conducting the FIB-HRSEM, Dr Alexander Gladkikh for performing the TOF-SIMS analysis, Dr Davide Levy for the XRD analysis, and Dr Pini Shekhter the XPS measurements.

References

1 J. Xu, X. Cai, S. Cai, Y. Shao, C. Hu, S. Lu and S. Ding, High-Energy Lithium-Ion Batteries: Recent Progress and a Promising Future in Applications, *Energy Environ. Mater.*, 2023, **6**, 1–26.
2 G. Berckmans, M. Messagie, J. Smekens, N. Omar, L. Vanhaverbeke and J. Van Mierlo, Cost projection of state of the art lithium-ion batteries for electric vehicles up to 2030, *Energies*, 2017, **10**, 1314, DOI: **10.3390/en10091314**.
3 F. M. N. U. Khan, M. G. Rasul, A. S. M. Sayem and N. K. Mandal, Design and optimization of lithium-ion battery as an efficient energy storage device for electric vehicles: A comprehensive review, *J. Energy Storage*, 2023, **71**, 108033.
4 M. Li, J. Lu, Z. Chen and K. Amine, 30 Years of Lithium-Ion Batteries, *Adv. Mater.*, 2018, **30**, 1–24.
5 A. Manthiram, J. C. Knight, S. T. Myung, S. M. Oh and Y. K. Sun, Nickel-Rich and Lithium-Rich Layered Oxide Cathodes: Progress and Perspectives, *Adv. Energy Mater.*, 2016, **6**, 1501010, DOI: **10.1002/aenm.201501010**.
6 W. Liu, P. Oh, X. Liu, M. J. Lee, W. Cho, S. Chae, Y. Kim and J. Cho, Nickel-Rich Layered Lithium Transition-Metal Oxide for High-Energy Lithium-Ion Batteries, *Angew. Chem., Int. Ed.*, 2015, **54**, 4440–4457.
7 W. Lee, S. Muhammad, C. Sergey, H. Lee, J. Yoon, Y. M. Kang and W. S. Yoon, Advances in the Cathode Materials for Lithium Rechargeable Batteries, *Angew. Chem., Int. Ed.*, 2020, **59**, 2578–2605.
8 N. Nitta, F. Wu, J. T. Lee and G. Yushin, Li-ion battery materials: Present and future, *Mater. Today*, 2015, **18**, 252–264.
9 H. Sun and K. Zhao, Electronic Structure and Comparative Properties of LiNixMnyCozO2 Cathode Materials, *J. Phys. Chem. C*, 2017, **121**, 6002–6010.
10 H. J. Noh, S. Youn, C. S. Yoon and Y. K. Sun, Comparison of the structural and electrochemical properties of layered Li[NixCoyMnz]O2 (x = 1/3, 0.5, 0.6, 0.7, 0.8 and 0.85) cathode material for lithium-ion batteries, *J. Power Sources*, 2013, **233**, 121–130.
11 N. Zhang, J. Li, H. Li, A. Liu, Q. Huang, L. Ma, Y. Li and J. R. Dahn, Structural, Electrochemical, and Thermal Properties of Nickel-Rich LiNixMnyCozO2 Materials, *Chem. Mater.*, 2018, **30**, 8852–8860.
12 A. Chakraborty, S. Kunnikuruvan, S. Kumar, B. Markovsky, D. Aurbach, M. Dixit and D. T. Major, Layered Cathode Materials for Lithium-Ion Batteries: Review of Computational Studies on LiNi1−x−yCoxMnyO2 and LiNi1−x−yCoxAlyO2, *Chem. Mater.*, 2020, **32**, 915–952.
13 X. Zeng, M. Li, D. Abd El-Hady, W. Alshitari, A. S. Al-Bogami, J. Lu and K. Amine, Commercialization of Lithium Battery Technologies for Electric Vehicles, *Adv. Energy Mater.*, 2019, **9**, 1900161, DOI: **10.1002/aenm.201900161**.
14 Y. K. Sun, High-Capacity Layered Cathodes for Next-Generation Electric Vehicles, *ACS Energy Lett.*, 2019, **4**, 1042–1044.
15 J. Dunn, M. Slattery, A. Kendall, H. Ambrose and S. Shen, Circularity of Lithium-Ion Battery Materials in Electric Vehicles, *Environ. Sci. Technol.*, 2021, **55**, 5189–5198.
16 M. S. Whittingham and J. Xiao, Fifty years of lithium-ion batteries and what is next?, *MRS Bull.*, 2023, **48**, 1118–1124.
17 M. Jiang, D. L. Danilov, R. A. Eichel and P. H. L. Notten, A Review of Degradation Mechanisms and Recent Achievements for Ni-Rich Cathode-Based Li-Ion Batteries, *Adv. Energy Mater.*, 2021, **11**, 2103005, DOI: **10.1002/aenm.202103005**.
18 S. S. Zhang, Problems and their origins of Ni-rich layered oxide cathode materials, *Energy Storage Mater.*, 2020, **24**, 247–254.
19 D. Das, S. Manna and S. Puravankara, Electrolytes, Additives and Binders for NMC Cathodes in Li-Ion Batteries—A Review, *Batteries*, 2023, **9**, 193, DOI: **10.3390/batteries9040193**.
20 G. L. Xu, X. Liu, A. Daali, R. Amine, Z. Chen and K. Amine, Challenges and Strategies to Advance High-Energy Nickel-Rich Layered Lithium Transition Metal Oxide Cathodes for Harsh Operation, *Adv. Funct. Mater.*, 2020, **30**, 2004748.
21 T. Li, X. Z. Yuan, L. Zhang, D. Song, K. Shi and C. Bock, *Degradation Mechanisms and Mitigation Strategies of Nickel-Rich NMC-Based Lithium-Ion Batteries*, Springer Singapore, 2020, vol. 3, pp. 43–80.
22 S. Bak, E. Hu, Y. Zhou, X. Yu, S. D. Senanayake, S. Cho, K. Kim, K. Y. Chung, X. Yang and K. Nam, Structural Changes and Thermal Stability of Charged LiNixMnyCozO2 Cathode Materials Studied by Combined In Situ Time-Resolved XRD and Mass Spectroscopy, *ACS Appl. Mater. Interfaces*, 2014, **6**, 22594–22601.

23 R. Jung, F. Linsenmann, R. Thomas, J. Wandt, S. Solchenbach, F. Maglia, C. Stinner, M. Tromp and H. A. Gasteiger, Nickel, Manganese, and Cobalt Dissolution from Ni-Rich NMC and Their Effects on NMC622-Graphite Cells, *J. Electrochem. Soc.*, 2019, **166**, A378–A389.

24 W. Choi and A. Manthiram, Comparison of Metal Ion Dissolutions from Lithium Ion Battery Cathodes, *J. Electrochem. Soc.*, 2006, **153**, A1760.

25 J. Li, G. Liang, W. Zheng, S. Zhang, K. Davey, W. Kong and Z. Guo, Addressing cation mixing in layered structured cathodes for lithium-ion batteries: A critical review, *Nano Mater. Sci.*, 2023, **5**, 404–420, DOI: **10.1016/j.nanoms.2022.09.001**.

26 Q. Gan, N. Qin, H. Yuan, L. Lu, Z. Xu and Z. Lu, Insight into the active sites of M–N–C single-atom catalysts for electrochemical CO_2 reduction, *EnergyChem*, 2023, **5**, 100114.

27 R. Jung, M. Metzger, F. Maglia, C. Stinner and H. A. Gasteiger, Oxygen Release and Its Effect on the Cycling Stability of LiNix MnyCozO2 (NMC) Cathode Materials for Li-Ion Batteries, *J. Electrochem. Soc.*, 2017, **164**, A1361–A1377.

28 D.-H. Cho, C.-H. Jo, W. Cho, Y.-J. Kim, H. Yashiro, Y.-K. Sun and S.-T. Myung, Effect of Residual Lithium Compounds on Layer Ni-Rich Li[Ni 0.7 Mn 0.3]O 2, *J. Electrochem. Soc.*, 2014, **161**, A920–A926.

29 R. Zhang, S. Yang, H. Li, T. Zhai and H. Li, Air sensitivity of electrode materials in Li/Na ion batteries: Issues and strategies, *InfoMat*, 2022, **4**, 1–26.

30 N. Zhang, B. Wang, F. Jin, Y. Chen, Y. Jiang, C. Bao, J. Tian, J. Wang, R. Xu, Y. Li, Q. Lv, H. Ren, D. Wang, H. Liu, S. Dou and X. Hong, Modified cathode-electrolyte interphase toward high-performance batteries, *Cell Rep. Phys. Sci.*, 2022, **3**, 101197, DOI: **10.1016/j.xcrp.2022.101197**.

31 J. Xu, Critical Review on cathode–electrolyte Interphase Toward High-Voltage Cathodes for Li-Ion Batteries, *Nano-Micro Lett.*, 2022, **14**, 166, DOI: **10.1007/s40820-022-00917-2**.

32 J. Cabana, B. J. Kwon and L. Hu, Mechanisms of Degradation and Strategies for the Stabilization of Cathode-Electrolyte Interfaces in Li-Ion Batteries, *Acc. Chem. Res.*, 2018, **51**, 299–308.

33 J. C. Stallard, L. Wheatcroft, S. G. Booth, R. Boston and S. A. Corr, Mechanical properties of cathode materials for lithium-ion batteries, *Joule*, 2022, **6**, 984–1007.

34 S. Yin, W. Deng, J. Chen, X. Gao, G. Zou, H. Hou and X. Ji, Fundamental and solutions of microcrack in Ni-rich layered oxide cathode materials of lithium-ion batteries, *Nano Energy*, 2021, **83**, 105854, DOI: **10.1016/j.nanoen.2021.105854**.

35 P. V. Chombo and Y. Laoonual, A review of safety strategies of a Li-ion battery, *J. Power Sources*, 2020, **478**, 228649.

36 E. Peled, D. Golodnitsky and G. Ardel, Advanced Model for Solid Electrolyte Interphase Electrodes in Liquid and Polymer Electrolytes, *J. Electrochem. Soc.*, 1997, **144**, L208–L210.

37 H. Xu, Q. Yan, W. Yao, C.-S. Lee and Y. Tang, Mainstream Optimization Strategies for Cathode Materials of Sodium-Ion Batteries, *Small Struct.*, 2022, **3**, 2100217.

38 A. Butt, G. Ali, K. Tul Kubra, R. Sharif, A. Salman, M. Bashir and S. Jamil, Recent Advances in Enhanced Performance of Ni-Rich Cathode Materials for Li-Ion Batteries: A Review, *Energy Technol.*, 2022, **10**, 2100775, DOI: **10.1002/ente.202100775**.

39 P. Teichert, G. G. Eshetu, H. Jahnke and E. Figgemeier, Degradation and aging routes of Ni-rich cathode based Li-ion batteries, *Batteries*, 2020, **6**, 1–26.

40 Z. Ahaliabadeh, X. Kong, E. Fedorovskaya and T. Kallio, Extensive comparison of doping and coating strategies for Ni-rich positive electrode materials, *J. Power Sources*, 2022, **540**, 231633.

41 M. J. Herzog, D. Esken and J. Janek, Improved Cycling Performance of High-Nickel NMC by Dry Powder Coating with Nanostructured Fumed Al2O3, TiO2, and ZrO2: A Comparison, *Batteries Supercaps*, 2021, **4**, 1003–1017.

42 S. Maiti, H. Sclar, R. Sharma, N. Vishkin, M. Fayena-Greenstein, J. Grinblat, M. Talianker, L. Burstein, N. Solomatin, O. Tiurin, Y. Ein-Eli, M. Noked, B. Markovsky and D. Aurbach, Understanding the Role of Alumina (Al2O3), pentalithium Aluminate (Li5AlO4), and pentasodium Aluminate (Na5AlO4) Coatings on the Li and Mn-Rich NCM Cathode Material 0.33Li2MnO3·0.67Li(Ni0.4Co0.2Mn0.4)O2 for Enhanced Electrochemical Performance, *Adv. Funct. Mater.*, 2021, **31**, 2008083, DOI: **10.1002/adfm.202008083**.

43 S. Tubtimkuna, N. Phattharasupakun, P. Bunyanidhi and M. Sawangphruk, Diffusion of Zirconium (IV) Ions from Coated Thick Zirconium Oxide Shell to the Bulk Structure of Ni-Rich NMC811 Cathode Leading to High-Performance 18650 Cylindrical Li-Ion Batteries, *Adv. Mater. Technol.*, 2022, **7**, 1–11.

44 K. Liu, Q. Zhang, S. Dai, W. Li, X. Liu, F. Ding and J. Zhang, Synergistic Effect of F- Doping and LiF Coating on Improving the High-Voltage Cycling Stability and Rate Capacity of LiNi0.5Co0.2Mn0.3O2 Cathode Materials for Lithium-Ion Batteries, *ACS Appl. Mater. Interfaces*, 2018, **10**, 34153–34162.

45 S. Dai, G. Yan, L. Wang, L. Luo, Y. Li, Y. Yang, H. Liu, Y. Liu and M. Yuan, Enhanced electrochemical performance and thermal properties of Ni-rich LiNi0.8Co0.1Mn0.1O2 cathode material via CaF2 coating, *J. Electroanal. Chem.*, 2019, **847**, 113197.

46 L. Sharma, M. Yi, E. Jo, H. Celio and A. Manthiram, Surface Stabilization with Fluorine of Layered Ultrahigh-Nickel Oxide Cathodes for Lithium-Ion Batteries, *Chem. Mater.*, 2022, **34**, 4514–4522, DOI: **10.1021/acs.chemmater.2c00301**.

47 S. H. Akella, S. Taragin, Y. Wang, H. Aviv, A. C. Kozen, M. Zysler, L. Wang, D. Sharon, S. B. Lee and M. Noked, Improvement of the Electrochemical Performance of LiNi0.8Co0.1Mn0.1O2 via Atomic Layer Deposition of Lithium-Rich Zirconium Phosphate Coatings, *ACS Appl. Mater. Interfaces*, 2021, **13**, 61733–61741.

48 M. Bandpey, M. Dorri, A. Babaei, C. Zamani and M. Bortolotti, Improved Electrochemical Performance of the Cation-Disordered NMC Cathode of Lithium-Ion Batteries by Lithium Phosphate Coating, *ACS Appl. Energy Mater.*, 2023, **6**, 7974–7984.

49 H. Dong, D. Sun, M. Xie, M. Cai, Z. Zhang, T. Cai, W. Dong and F. Huang, A uniform and high-voltage stable LiTMPO4 coating layer enabled high performance LiNi0.8Co0.15Mn0.05O2 towards boosting lithium storage, *Dalton Trans.*, 2022, **51**, 12532–12539.

50 L. Liang, X. Sun, C. Wu, L. Hou, J. Sun, X. Zhang and C. Yuan, Nasicon-Type Surface Functional Modification in Core-Shell LiNi0.5Mn0.3Co0.2O2@NaTi2(PO4)3 Cathode Enhances Its High-Voltage Cycling Stability and Rate Capacity toward Li-Ion Batteries, *ACS Appl. Mater. Interfaces*, 2018, **10**, 5498–5510.

51 Y. Liang, J. Cai, D. Liu and Z. Chen, Surface Modification of Nickel-Rich Cathode Materials by Ionically Conductive Materials at Room Temperature, *Energy Technol.*, 2021, **9**, 1–7.

52 S. K. Singh, D. P. Dutta, H. Gupta, N. Srivastava, R. Mishra, D. Meghnani, R. K. Tiwari, A. Patel, A. Tiwari and R. K. Singh, Electrochemical investigation of double layer surface-functionalized Li-NMC cathode with nano-composite gel polymer electrolyte for Li-battery applications, *Electrochim. Acta*, 2022, **435**, 141328.

53 S. Chen, T. He, Y. Su, Y. Lu, L. Bao, L. Chen, Q. Zhang, J. Wang, R. Chen and F. Wu, Ni-Rich LiNi0.8Co0.1Mn0.1O2 Oxide Coated by Dual-Conductive Layers as High Performance Cathode Material for Lithium-Ion Batteries, *ACS Appl. Mater. Interfaces*, 2017, **9**, 29732–29743.

54 Y. Cao, X. Qi, K. Hu, Y. Wang, Z. Gan, Y. Li, G. Hu, Z. Peng and K. Du, Conductive Polymers Encapsulation to Enhance Electrochemical Performance of Ni-Rich Cathode Materials for Li-Ion Batteries, *ACS Appl. Mater. Interfaces*, 2018, **10**, 18270–18280.

55 Q. Hou, G. Cao, P. Wang, D. Zhao, X. Cui, S. Li and C. Li, Carbon coating nanostructured-LiNi1/3Co1/3Mn1/3O2 cathode material synthesized by chemical vapor deposition method for high performance lithium-ion batteries, *J. Alloys Compd.*, 2018, **747**, 796–802.

56 Z. Wu, S. Ji, T. Liu, Y. Duan, S. Xiao, Y. Lin, K. Xu and F. Pan, Aligned Li+ Tunnels in Core-Shell Li(NixMnyCoz) O2@LiFePO4 Enhances Its High Voltage Cycling Stability as Li-ion Battery Cathode, *Nano Lett.*, 2016, **16**, 6357–6363.

57 X. Lin, Y. Sun, Y. Liu, K. Jiang and A. Cao, Stabilization of high-energy cathode materials of metal-ion batteries: Control strategies and synthesis protocols, *Energy Fuels*, 2021, **35**, 7511–7527.

58 D. Zuo, G. Tian, X. Li, D. Chen and K. Shu, Recent progress in surface coating of cathode materials for lithium ion secondary batteries, *J. Alloys Compd.*, 2017, **706**, 24–40.

59 B. Xiao and X. Sun, Surface and Subsurface Reactions of Lithium Transition Metal Oxide Cathode Materials: An Overview of the Fundamental Origins and Remedying Approaches, *Adv. Energy Mater.*, 2018, **8**, 1–27.

60 G. Kaur and B. D. Gates, Review—Surface Coatings for Cathodes in Lithium Ion Batteries: From Crystal Structures to Electrochemical Performance, *J. Electrochem. Soc.*, 2022, **169**, 043504.

61 M. J. Herzog, N. Gauquelin, D. Esken, J. Verbeeck and J. Janek, Facile Dry Coating Method of High-Nickel Cathode Material by Nanostructured Fumed Alumina (Al2O3) Improving the Performance of Lithium-Ion Batteries, *Energy Technol.*, 2021, **9**, 2100028, DOI: **10.1002/ente.202100028**.

62 J. Ahn, E. K. Jang, S. Yoon, S. J. Lee, S. J. Sung, D. H. Kim and K. Y. Cho, Ultrathin ZrO2 on LiNi0.5Mn0.3Co0.2O2 electrode surface via atomic layer deposition for high-voltage operation in lithium-ion batteries, *Appl. Surf. Sci.*, 2019, **484**, 701–709.

63 Y. J. Kim, S. Y. Ko, S. Kim, K. M. Choi and W. H. Ryu, Cathodes Coating Layer with Li-Ion Diffusion Selectivity Employing Interactive Network of Metal-Organic Polyhedras for Li-Ion Batteries, *Small*, 2022, **2206561**, 1–12.

64 X. Wang and G. Yushin, Chemical vapor deposition and atomic layer deposition for advanced lithium ion batteries and supercapacitors, *Energy Environ. Sci.*, 2015, **8**, 1889–1904.

65 D. Zuo, G. Tian, X. Li, D. Chen and K. Shu, Recent progress in surface coating of cathode materials for lithium ion secondary batteries, *J. Alloys Compd.*, 2017, **706**, 24–40.

66 M. A. Butt, Thin-film coating methods: a successful marriage of high-quality and cost-effectiveness-A brief exploration, *Coatings*, 2022, **12**, 1115, DOI: **10.20944/preprints202207.0177.v1**.

67 A. Kausar, Polymer coating technology for high performance applications: Fundamentals and advances, *J. Macromol. Sci., Part A:Pure Appl. Chem.*, 2018, **55**, 440–448.

68 H. C. Hamaker, Formation O F A Deposit By Electro-Phoresis, *Trans. Faraday Soc.*, 1940, **35**, 279–287.

69 P. Sarkar and P. S. Nicholson, *J. Am. Ceram. Soc.*, 1996, **79**, 1987–2002.

70 B. Ferrari and R. Moreno, EPD kinetics: A review, *J. Eur. Ceram. Soc.*, 2010, **30**, 1069–1078.

71 A. Hajizadeh, T. Shahalizade, R. Riahifar, M. S. Yaghmaee, B. Raissi, S. Gholam, A. Aghaei, S. Rahimisheikh and A. S. Ghazvini, Electrophoretic deposition as a fabrication method for Li-ion battery electrodes and separators – A review, *J. Power Sources*, 2022, **535**, 231448.

72 X. Cheng, Y. Liu, O. Liu, Y. Lu, A. R. Boccaccini and F. Yang, Progress in Materials Science Electrophoretic deposition of coatings for local delivery of therapeutic agents, *Prog. Mater. Sci.*, 2023, **136**, 101111.

73 R. Sikkema, K. Baker and I. Zhitomirsky, Electrophoretic deposition of polymers and proteins for biomedical applications, *Adv. Colloid Interface Sci.*, 2020, **284**, 102272.

74 L. Besra and M. Liu, A review on fundamentals and applications of electrophoretic deposition (EPD), *Prog. Mater. Sci.*, 2007, **52**, 1–61.

75 P. Cao, B. Li, G. Yang, S. Zhao, J. Townsend, K. Xing, Z. Qiang, K. D. Vogiatzis, A. P. Sokolov, J. Nanda and T. Saito, Elastic Single-Ion Conducting Polymer Electrolytes: Toward

a Versatile Approach for Intrinsically Stretchable Functional Polymers, *Macromolecules*, 2020, **53**, 3591–3601, DOI: **10.1021/acs.macromol.9b02683**.

76 S. Zhao, Y. Zhang, H. Pham, J. Y. Carrillo, B. G. Sumpter, J. Nanda, N. J. Dudney, T. Saito, A. P. Sokolov and P. Cao, Improved Single-Ion Conductivity of Polymer Electrolyte via Accelerated Segmental Dynamics, *ACS Appl. Energy Mater.*, 2020, **3**, 12540–12548, DOI: **10.1021/acsaem.0c02079**.

77 J. Yuan, D. Mecerreyes and M. Antonietti, Poly(ionic liquid) s: An update, *Prog. Polym. Sci.*, 2013, **38**, 1009–1036.

78 C. Li, S. Zhang, X. Miao, C. Wang and C. Wang, Designing Lithium Argyrodite Solid-State Electrolytes for High-Performance All-Solid-State Lithium Batteries, *Batteries Supercaps*, 2022, **5**, 14–39.

79 H. J. Deiseroth, S. T. Kong, H. Eckert, J. Vannahme, C. Reiner, T. Zaiß and M. Schlosser, Li6PS5X: A class of crystalline Li-rich solids with an unusually high Li+ mobility, *Angew. Chem., Int. Ed.*, 2008, **47**, 755–758.

80 D. H. S. Tan, E. A. Wu, H. Nguyen, Z. Chen, M. A. T. Marple, J. Doux, X. Wang, H. Yang, A. Banerjee and Y. S. Meng, Elucidating Reversible Electrochemical Redox of Li6PS5Cl Solid Electrolyte, *ACS Energy Lett.*, 2019, **4**, 2418–2427.

81 J. Auvergniot, A. Cassel, J. B. Ledeuil, V. Viallet, V. Seznec and R. Dedryvère, Interface Stability of Argyrodite Li6PS5Cl toward LiCoO2, LiNi1/3Co1/3Mn1/3O2, and LiMn2O4 in Bulk All-Solid-State Batteries, *Chem. Mater.*, 2017, **29**, 3883–3890.

82 S. Wang, M. Tang, Q. Zhang, B. Li, S. Ohno, F. Walther, R. Pan, X. Xu, C. Xin, W. Zhang, L. Li, Y. Shen, F. H. Richter, J. Janek and C. W. Nan, Lithium Argyrodite as Solid Electrolyte and Cathode Precursor for Solid-State Batteries with Long Cycle Life, *Adv. Energy Mater.*, 2021, **11**, 2101370, DOI: **10.1002/aenm.202101370**.

83 T. Zuo, F. Walther, S. Ahmed, R. Rueß, J. Hertle, B. Mogwitz, K. Volz and J. Janek, Formation of an Artificial Cathode–Electrolyte Interphase to Suppress Interfacial Degradation of Ni-Rich Cathode Active Material with Sulfide Electrolytes for Solid-State Batteries, *ACS Energy Lett.*, 2023, **8**, 1322–1329.

84 T. H. Wan, M. Saccoccio, C. Chen and F. Ciucci, Influence of the Discretization Methods on the Distribution of Relaxation Times Deconvolution: Implementing Radial Basis Functions with DRTtools, *Electrochim. Acta*, 2015, **184**, 483–499.

85 A. Maradesa, B. Py, T. H. Wan, M. B. Effat and F. Ciucci, Selecting the Regularization Parameter in the Distribution of Relaxation Times, *J. Electrochem. Soc.*, 2023, **170**, 030502.

86 J. Auvergniot, A. Cassel, D. Foix, V. Viallet, V. Seznec and R. Dedryvère, Redox activity of argyrodite Li6PS5Cl electrolyte in all-solid-state Li-ion battery: An XPS study, *Solid State Ionics*, 2017, **300**, 78–85.

87 Ö. U. Kudu, T. Famprikis, B. Fleutot, M. D. Braida, T. Le Mercier, M. S. Islam and C. Masquelier, A review of structural properties and synthesis methods of solid electrolyte materials in the Li2S – P2S5 binary system, *J. Power Sources*, 2018, **407**, 31–43.

88 H. Stöffler, T. Zinkevich, M. Yavuz, A. L. Hansen, M. Knapp, J. Bednarčík, S. Randau, F. H. Richter, J. Janek, H. Ehrenberg and S. Indris, Amorphous versus Crystalline Li3PS4: Local Structural Changes during Synthesis and Li Ion Mobility, *J. Phys. Chem. C*, 2019, **123**, 10280–10290.

89 M. Calpa, N. C. Rosero-Navarro, A. Miura, K. Terai, F. Utsuno and K. Tadanaga, Formation mechanism of thiophosphate anions in the liquid-phase synthesis of sulfide solid electrolytes using polar aprotic solvents, *Chem. Mater.*, 2020, **32**, 9627–9632.

90 S. Cui, Y. Wei, T. Liu, W. Deng, Z. Hu, Y. Su, H. Li, M. Li, H. Guo, Y. Duan, W. Wang, M. Rao, J. Zheng, X. Wang and F. Pan, Optimized Temperature Effect of Li-Ion Diffusion with Layer Distance in Li (NixMnyCoz)O2 Cathode Materials for High Performance Li-Ion Battery, *Adv. Energy Mater.*, 2016, **6**, 1501309, DOI: **10.1002/aenm.201501309**.

91 H. Khan, A. S. Yerramilli, A. D'Oliveira, T. L. Alford, D. C. Boffito and G. S. Patience, Experimental methods in chemical engineering: X-ray diffraction spectroscopy—XRD, *Can. J. Chem. Eng.*, 2020, **98**, 1255–1266.

92 Y. Wang, Z. Yang, Y. Qian, L. Gu and H. Zhou, New Insights into Improving Rate Performance of Lithium-Rich Cathode Material, *Adv. Mater.*, 2015, **27**, 3915–3920.

93 S. B. Kim, H. Kim, D. H. Park, J. H. Kim, J. H. Shin, J. S. Jang, S. H. Moon, J. H. Choi and K. W. Park, Li-ion diffusivity and electrochemical performance of Ni-rich cathode material doped with fluoride ions, *J. Power Sources*, 2021, **506**, 230219, DOI: **10.1016/j.jpowsour.2021.230219**.

94 K. Ben-Kamel, N. Amdouni, A. Mauger and C. M. Julien, Study of the local structure of LiNi 0.33+δMn 0.33+δCo 0.33-2δO 2 (0.025 ≤ δ ≤ 0.075) oxides, *J. Alloys Compd.*, 2012, **528**, 91–98.

95 C. Ghanty, B. Markovsky, E. M. Erickson, M. Talianker, O. Haik, Y. Tal-Yossef, A. Mor, D. Aurbach, J. Lampert, A. Volkov, J. Y. Shin, A. Garsuch, F. F. Chesneau and C. Erk, Li +-Ion Extraction/Insertion of Ni-Rich Li1+x(NiyCozMnz)wO2 (0.005<x<0.03; y: Z=8:1, w≈1) Electrodes: In Situ XRD and Raman Spectroscopy Study, *ChemElectroChem*, 2015, **2**, 1479–1486.

96 X. Zhang, A. Mauger, Q. Lu, H. Groult, L. Perrigaud, F. Gendron and C. M. Julien, Synthesis and characterization of LiNi1/3Mn1/3Co 1/3O2 by wet-chemical method, *Electrochim. Acta*, 2010, **55**, 6440–6449.

97 F. Kong, C. Liang, R. C. Longo, D. H. Yeon, Y. Zheng, J. H. Park, S. G. Doo and K. Cho, Conflicting roles of anion doping on the electrochemical performance of Li-ion battery cathode materials, *Chem. Mater.*, 2016, **28**, 6942–6952.

98 S. H. Park, Y.-K. Sun, K. S. Park, K. S. Nahm, Y. S. Lee and M. Yoshio, Synthesis and electrochemical properties of lithium nickel oxysulfide (LiNiSyO2-y) material for lithium secondary batteries, *Electrochim. Acta*, 2002, **47**, 1721–1726.

99 X. Li, F. Kang, W. Shen and X. Bai, Improvement of structural stability and electrochemical activity of a cathode material LiNi0.7Co0.3O2 by chlorine doping, *Electrochim. Acta*, 2007, **53**, 1761–1765.

100 P. Iurilli, C. Brivio and V. Wood, On the use of electrochemical impedance spectroscopy to characterize and model the aging phenomena of lithium-ion batteries: a critical review, *J. Power Sources*, 2021, **505**, 229860.
101 J. B. Goodenough and K. Park, The Li-Ion Rechargeable Battery : A Perspective, *J. Am. Chem. Soc.*, 2013, **135**, 1167–1176.
102 C. Liu, Z. G. Neale and G. Cao, *Mater. Today*, 2016, **19**, 109–123.
103 F. Li, R. Liu, J. Liu and H. Li, Voltage Hysteresis in Transition Metal Oxide Cathodes for Li / Na-Ion Batteries, *Adv. Funct. Mater.*, 2023, **33**, 2300602.
104 A. Van Der Ven, K. A. See and L. Pilon, Hysteresis in electrochemical systems, *Battery Energy*, 2022, **1**, 20210017, DOI: **10.1002/bte2.20210017**.
105 W. Li, L. M. Housel, G. P. Wheeler, D. C. Bock, K. J. Takeuchi, E. S. Takeuchi and A. C. Marschilok, Thermodynamic Analysis of LiNi0.6Mn0.2Co0.2O2 (NMC622) Voltage Hysteresis Induced through High Voltage Charge, *ACS Appl. Energy Mater.*, 2021, **4**, 12067–12073.
106 M. J. Herzog, N. Gauquelin, D. Esken, J. Verbeeck and J. Janek, Increased Performance Improvement of Lithium-Ion Batteries by Dry Powder Coating of High-Nickel NMC with Nanostructured Fumed Ternary Lithium Metal Oxides, *ACS Appl. Energy Mater.*, 2021, **4**, 8832–8848, DOI: **10.1021/acsaem.1c00939**.
107 P. Iurilli, C. Brivio and V. Wood, Detection of Lithium-Ion Cells' Degradation through Deconvolution of Electrochemical Impedance Spectroscopy with Distribution of Relaxation Time, *Energy Technol.*, 2022, **10**, 2200547, DOI: **10.1002/ente.202200547**.
108 Y. Zhao, V. Kumtepeli, S. Ludwig and A. Jossen, Investigation of the distribution of relaxation times of a porous electrode using a physics-based impedance model, *J. Power Sources*, 2022, **50**, 231250, DOI: **10.1016/j.jpowsour.2022.231250**.
109 X. Chen, L. Li, M. Liu, T. Huang and A. Yu, Detection of lithium plating in lithium-ion batteries by distribution of relaxation times, *J. Power Sources*, 2021, **496**, 229867, DOI: **10.1016/j.jpowsour.2021.229867**.
110 K. N. Wood, K. X. Steirer, S. E. Hafner, C. Ban, S. Santhanagopalan, S. H. Lee and G. Teeter, Operando X-ray photoelectron spectroscopy of solid electrolyte interphase formation and evolution in Li2S-P2S5 solid-state electrolytes, *Nat. Commun.*, 2018, **9**, 2490, DOI: **10.1038/s41467-018-04762-z**.
111 J. Liang, X. Li, Y. Zhao, L. V. Goncharova, G. Wang, K. R. Adair, C. Wang, R. Li, Y. Zhu, Y. Qian, L. Zhang, R. Yang, S. Lu and X. Sun, In Situ Li3PS4 Solid-State Electrolyte Protection Layers for Superior Long-Life and High-Rate Lithium-Metal Anodes, *Adv. Mater.*, 2018, **30**, 1804684, DOI: **10.1002/adma.201804684**.
112 H. Wang, L. Wu, B. Xue, F. Wang, Z. Luo, X. Zhang, L. Calvez, P. Fan and B. Fan, Improving Cycling Stability of the Lithium Anode by a Spin-Coated High-Purity Li3PS4 Artificial SEI Layer, *ACS Appl. Mater. Interfaces*, 2022, **14**, 15214–15224.
113 J. Xu, J. Li, Y. Li, M. Yang, L. Chen, H. Li and F. Wu, Long-Life Lithium-Metal All-Solid-State Batteries and Stable Li Plating Enabled by In Situ Formation of Li3PS4 in the SEI Layer, *Adv. Mater.*, 2022, **34**, 2203281, DOI: **10.1002/adma.202203281**.
114 X. B. Cheng, R. Zhang, C. Z. Zhao, F. Wei, J. G. Zhang and Q. Zhang, A review of solid electrolyte interphases on lithium metal anode, *Adv. Sci.*, 2015, **3**, 1500213, DOI: **10.1002/advs.201500213**.
115 J. Tan, J. Matz, P. Dong, J. Shen and M. Ye, A Growing Appreciation for the Role of LiF in the Solid Electrolyte Interphase, *Adv. Energy Mater.*, 2021, **11**, 2100046, DOI: **10.1002/aenm.202100046**.
116 L. Wang, A. Mukherjee, C. Y. Kuo, S. Chakrabarty, R. Yemini, A. A. Dameron, J. W. DuMont, S. H. Akella, A. Saha, S. Taragin, H. Aviv, D. Naveh, D. Sharon, T. S. Chan, H. J. Lin, J. F. Lee, C. Te Chen, B. Liu, X. Gao, S. Basu, Z. Hu, D. Aurbach, P. G. Bruce and M. Noked, High-energy all-solid-state lithium batteries enabled by Co-free LiNiO2 cathodes with robust outside-in structures, *Nat. Nanotechnol.*, 2024, **19**, 208–218.
117 R. Hausbrand, G. Cherkashinin, H. Ehrenberg, M. Gröting, K. Albe, C. Hess and W. Jaegermann, Fundamental degradation mechanisms of layered oxide Li-ion battery cathode materials: Methodology, insights and novel approaches, *Mater. Sci. Eng., B*, 2015, **192**, 3–25.
118 A. Monshi, M. R. Foroughi and M. R. Monshi, Modified Scherrer Equation to Estimate More Accurately Nano-Crystallite Size Using XRD, *World J. Nano Sci. Eng.*, 2012, **02**, 154–160.